

## Growth and dissolution features in hydrothermal vein minerals – an example of Colombian emeralds, an SEM and element mapping study

For submission to Mineralogical Magazine, Special volume in honour of Ed S. Grew

Gerhard Franz<sup>1\*</sup>, Ferry Schiperski<sup>1</sup>, Vladimir Khomenko<sup>2</sup>, Ulrich Gernert<sup>3</sup>, and Jörg Nissen<sup>3</sup>

<sup>1</sup>Fachgebiet Angewandte Geochemie, Technische Universität Berlin, D-10623 Berlin, Germany; <sup>2</sup>M.P. Semenenko Institute of Geochemistry, Mineralogy and Ore Formation, The National Academy of Sciences of Ukraine, Kyiv, 03142, Ukraine; <sup>3</sup>Zentraleinrichtung Elektronenmikroskopie, Technische Universität Berlin, D-10623 Berlin, Germany

\*corresponding author: Gerhard Franz, gefra548@gmail.com

### Abstract

Beryl crystals from hydrothermal veins in the Colombian emerald mining district, were examined to understand their growth and dissolution processes. Chemical analysis reveals minor substitution of Al by Na, Mg, and the colouring elements V, Cr, and Fe. Growth features include characteristic indentations on (0001) and a ridge-and-valley structure on the second-order prism, which is also observed on rare conical growth faces. Zoning is the primary internal growth feature, investigated in cross sections parallel to the main growth directions, the *a*- and *c*-axes of beryl. All crystals show sector zoning, with enrichment of Na and Mg in the *c*-sector, while Al and most of the trace elements measured are concentrated in the *a*-sector. H<sub>2</sub>O and CO<sub>2</sub> molecules in the crystal structure were identified by infrared spectroscopy. Two types of H<sub>2</sub>O are present, with the H-H vector aligned (type I) and perpendicular (type II) to the *c*-axis, with H<sub>2</sub>O II predominant in the *c*-sector. CO<sub>2</sub> is present in both sectors, decreasing from core to rim, and is higher in the *a*-sector. Variable sector boundaries suggest irregular changes in the growth rate in the two growth directions. The substitution  $(^{VI}\text{Mg}^{+\text{channel}}\text{Na})_{c\text{-sector}} = (^{VI}\text{Al}^{+\text{channel}}\square)_{a\text{-sector}}$  creates a pattern of stripes, originating at the steps of the sector boundaries. Etch pits as a result of dissolution are arranged in chains, typically forming etching channels, but the overall amount of dissolution is minor. The arrangement of the etch pits indicates that they formed on dislocation bundles, which originate at the sector boundaries. The observations

indicate rapid crystallization with skeletal growth in [0001]. responsible for the distribution of elements in sectors, and are consistent with a closed-system behaviour in the veins.

Keywords: Beryl; emerald; chemical zoning; etch pits; growth features; conical growth; scanning electron microscopy

## 1 Introduction

The elemental and isotopic zoning of minerals is related to their growth and the investigation of zoning patterns in minerals has been demonstrated as an extremely useful tool to reconstruct not only changes in the external parameters P and T during their growth, but also to obtain information about mass transfer processes within a mineral and on absolute time constraints using in-situ isotopic dating techniques (e.g. Kohn, 2014, and references therein). Information about the growth process is also preserved in the realbau (real structure) of a crystal, i.e. its defect structure, such as point defects, screw and edge dislocations, and subgrain boundaries. These defects become visible in etched crystals, as dissolution preferentially acts on such defects. Freely grown crystals, either from the pegmatitic stage in open cavities, or from hydrothermal vein assemblages, may provide an opportunity to study dissolution phenomena if they have well-developed faces. On the macroscopic to microscopic scale, these dissolution phenomena primarily manifest as etch pits (EP), offering indirect insights into their growth history, which have been extensively studied, particularly in material science (e.g. Sunagawa, 2005; Lu et al, 2022).

Hydrothermal vein assemblages are a typical setting, where beryl ( $\text{Be}_3\text{Al}_2[\text{Si}_6\text{O}_{18}]$ ) occurs (Grew, 2002). Its green gemstone variety, emerald, has been extensively studied (e.g. Groat et al., 2008), also due to its pronounced zoning features. Etch pits (EP) as dissolution phenomena in beryl were investigated to explore their feasibility as provenance indicators (Kurumathoor and Franz, 2018; Franz et al., 2023), as a complementary tool to inclusion studies and chemical composition (Saeseaw et al., 2019). Growth conditions in terms of pressure, temperature, fluid composition, and time, can vary from locality to locality, as described by Scandale et al. (1990) for pegmatitic beryls. Consequently, the shape and arrangement of EP can be characteristic for a specific locality.

We selected beryl crystals from Colombia for our study, sourced from vein assemblages in a low-grade metasedimentary sequence of black shales, limestones and evaporites; temperature-pressure conditions of formation did not exceed approximately 300 – 350°C/200 – 300 MPa (e.g. Pignatelli et al., 2015, and references therein). The low temperature excludes significant re-equilibration by

diffusion, making the EP and zoning patterns feasible indicators of the realbau. The freely grown crystals show no indications for later deformation such as cracks or subgrain boundaries, and therefore no post-growth deformation modification of the zoning has occurred. According to the growth model for 'trapiche emeralds' (Pignatelli et al., 2015), these crystals formed due to sudden opening of veins during faulting and folding associated with extensional veins sets and hydraulic breccias. The basinal brines from the black shales transported the trace elements Be, V, and Cr, into the veins, which experienced a rapid pressure drop and a high oversaturation, possibly at near-peak metamorphic conditions.

Emerald samples were obtained from a mineral dealer in Bogotá, Colombia in 2014. Their exact sampling location remains unknown. Five crystals were examined in detail for this study. They exhibit both interior growth phenomena, such as chemical zoning of major and trace elements, analysed by element distribution maps, and characteristic surface features, analysed by scanning electron microscopy (SEM). These observations demonstrate rapid growth at strong disequilibrium conditions, resulting in pronounced sector zoning with complex sector boundaries. They indicate changes in relative growth rates parallel to the  $a$ - and  $c$ -axis, which differ entirely from those predicted for Rayleigh fractionation. Dissolution phenomena such as EP are minor, but distinct from those observed in pegmatitic beryls (Franz et al., 2023).

## **2. Methods**

A detailed description of the applied analytical methods is available in the supplementary material (Franz et al., 2025).

### **2.1 Scanning electron microscopy (SEM)**

Crystals were mounted on carbon tape, coated with a 16 nm thick carbon layer, and images were obtained using a Hitachi SU8030 cold-field emission SEM, equipped with a 30 mm<sup>2</sup> silicon drift detector (SDD) Octane-A Plus from EDAX for energy dispersive analysis (EDS) analysis. Images were obtained with an SE(L) detector, for low magnification in the low magnification mode (LM), some in combination with a back-scattered electron (BSE) detector.

### **2.2 $\mu$ -X-ray fluorescence ( $\mu$ XRF)**

After SEM imaging, the crystals were cut with a diamond-wire saw (wire diameter 60  $\mu$ m), parallel to their  $c$ - and  $a$ -directions through the centre of the crystals, aiming to achieve optimal visibility of zoning in cross sections. Crystal #4 was obtained as a fragment and could only be lapped by hand to

obtain a section parallel to  $[0001]\text{--}[11\bar{2}0]$ . To minimize mechanical damage, the (0001) face was covered with epoxy resin before sawing. Crystals were then fully embedded in epoxy for surface polishing.

We used the  $\mu$ -X-ray fluorescence energy dispersive spectrometer “M4 Tornado” (Bruker Nano GmbH) at the MAGMA Lab, TU Berlin, for generating element maps of the entire sectioned crystal for elements heavier than Na. Analyses were carried out in air. Steps were 20–50  $\mu\text{m}$  (equivalent to pixel size of the map) and an exposure time for each step of 20–100 ms was applied. The instrument is equipped with a Rh anode, a microfocus X-ray tube with Be window, operated at 50 kV and 600  $\mu\text{A}$ . Two 30  $\text{mm}^2$  silicon-drift detectors allow for an energy resolution (for Mn  $K\alpha$ ) of  $\leq 145$  eV.

### **2.3 Electron microprobe analysis (EMPA)**

The JEOL JXA-8530F field emission microprobe at TU Berlin was used for quantitative analyses and element mapping. The sections were carbon-coated and analysed in wave-length dispersive mode for Na, K, Ca, Mg, Mn, Fe, Al, Sc, V, Cr, Ti and Si. Detection limits for trace and minor elements were (in ppm) Fe 170, Mn 200, Cr 200, V 200, Ti 160, K 80, Ca 100, Rb 4500, Cs 110, Sc 55. Measuring conditions were 10/5 sec measuring time on peak/background, assuming a fixed BeO content of 13.16 wt% for ZAF correction, at 15 kV/20 nA probe current. From each crystal at least two representative analyses from core and rim were obtained. Formulae were calculated on the basis of 18 oxygen and adjusting the BeO value to Be = 3.000 cations per formula (cpfu). Inclusions were characterized by energy-dispersive analysis. BSE and secondary electron images (SEI) were obtained to gather information on inclusions and particularly on the trace of (0001) in cross section.

The whole-grain maps obtained by  $\mu\text{XRF}$  were used to select areas for more detailed EPMA mapping. Data for element distribution maps in the wave-length dispersive mode of the microprobe were acquired using 15 kV, 20 nA probe current, 100 nA for mapping, with a beam diameter of 10  $\mu\text{m}$ . Details about standards and measured X-ray lines are documented in the supplementary material. Mappings were performed in stage scan-modus with pixel resolution between  $280\text{--}600 \times 450\text{--}1000$  (depending on the total scan area, which was in the order of  $600 \mu\text{m} \times 2100 \mu\text{m}$ ), with a pixel size of mostly 2.12  $\mu\text{m}$ , and a dwell time per pixel of 100 ms. Data of background positions were not collected. Lateral and in-depth resolution was estimated by Monte-Carlo simulation as approximately 3.5  $\mu\text{m}$  and 2.5  $\mu\text{m}$ , respectively.

## 2.4 Infrared-spectroscopy (IR)

For IR spectroscopy, the same mounts used for  $\mu$ XRF and EMPA were ground to an approximate thickness of  $< 30\ \mu\text{m}$  from the reverse side, so that absorption in the region of fundamental vibrations ( $4000\text{--}1500\ \text{cm}^{-1}$ ) of  $\text{H}_2\text{O}$  and  $\text{CO}_2$  was sufficiently low to obtain spectra of high quality. A Bruker FTIR spectrometer IFS 66 equipped with an IR-microscope was used to obtain polarized spectra at room temperature in the spectral range  $7000\text{--}1000\ \text{cm}^{-1}$ . Spectra were scanned with a measuring spot of  $60\ \mu\text{m}$  diameter, at a spectral resolution of  $4\ \text{cm}^{-1}$ , and the time averaged signal was collected over 150–200 scans. The reference spectra were recorded in air.

## 3 Results

A complete set of all results – all SEM images, EDX spectra, IR spectra,  $\mu$ XRF mappings – is available in the supplementary material (Franz et al.; 2025).

### 3.1 Morphology of samples

The five crystals (Fig. 1) show a well-developed (0001) face and first-order prisms  $\{10\bar{1}0\}$ , some also smaller second-order prisms  $\{11\bar{2}0\}$ . Indentations on (0001) can be seen with a hand lens. The crystals are short prismatic, with an aspect ratio near one, only crystal #2 is elongated along the  $c$ -axis (Table 1). The base of the crystals is irregular, and only crystal #3 shows a very small amount of the rock matrix on which it grew. Colour varies between light green and dark green, indicating variable amounts of chromophore substitution. Crystal #5 shows conical growth (resembling sceptre growth) on one side of the crystal.

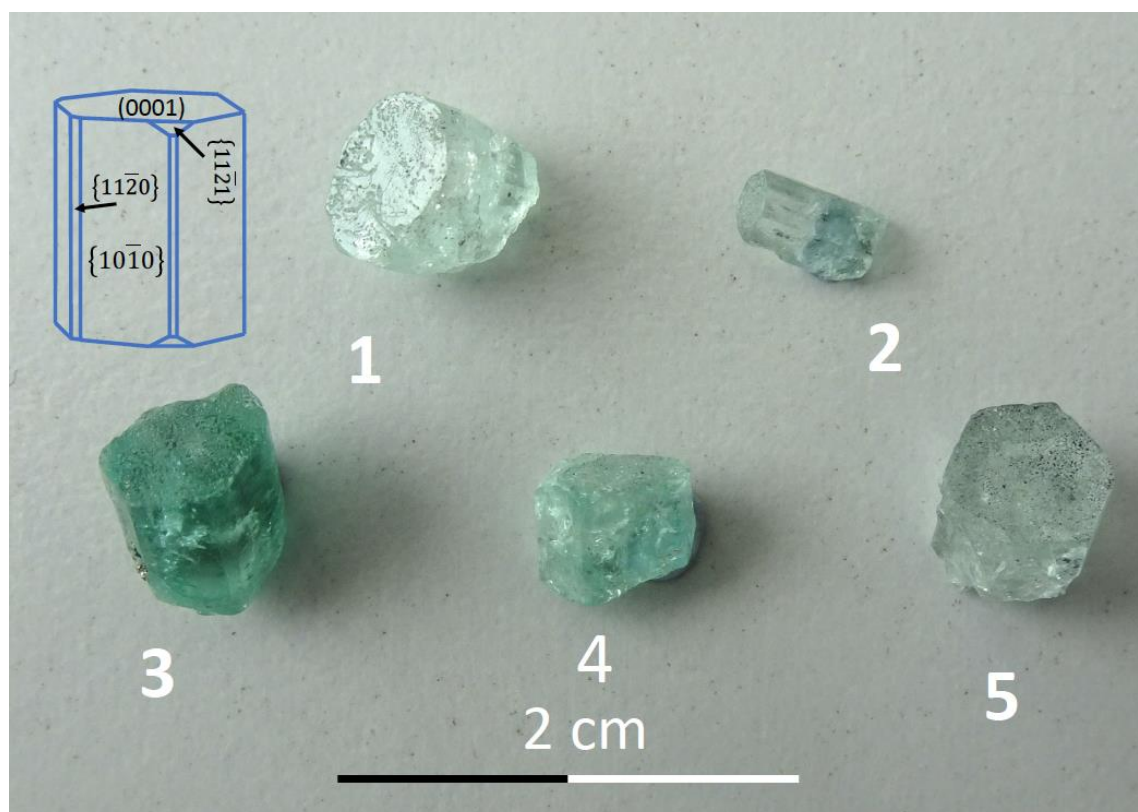


**Figure 1.** Photograph of the crystals and crystal drawing; in addition to the major faces (0001) and first-order prism  $\{10\bar{1}0\}$ , some crystals also showed the second-order prism  $\{11\bar{2}0\}$ ; only crystal #4 showed the hexagonal di-pyramid  $\{11\bar{2}1\}$ . None of the crystals shows the  $(000\bar{1})$  face.

**Table 1.** List of crystals, developed faces and approximate size

Crystal #	prism [mm]	(0001) [mm]	colour	$\{11\bar{2}0\}$	comment
2014-1	8	7	very light green	present	
2014-2	2	7	light green	present	
2014-3	7.5	8	dark green		pyrite inclusions
2014-4	7	5.5	light green	present	calcite inclusion $\{11\bar{2}1\}$ present
2014-5	8	8	very light green		conical growth

### 3.2 Composition

To characterise the beryl crystals, analyses by EMPA were obtained in representative areas, targeting to the largest difference seen in qualitative element distribution maps (for location of the analysis see figure in supplementary material. All analyses yielded at total between 99.03 and 100.89 wt%, indicating only minor amounts of undetectable components such as H<sub>2</sub>O at the channel position (Table 2). Calculation of the water content, using the formula by Henry et al. (2022), yields for an average value of 0.5 wt% Na<sub>2</sub>O 0.8 wt% H<sub>2</sub>O. They show a well-defined stoichiometry with a sum of octahedral cations between 1.896 and 2.090 cpfu (n = 13), Si(min) = 5.998 cpfu to Si(max) = 6.018 cpfu (calculated with the assumption Be = 3.000 cpfu), indicating near-ideal composition and no or only very minor substitution at the tetrahedral positions. Only Na and Mg, as substituents at the octahedral and channel positions, respectively, and present in equal amounts (in cpfu), show concentrations above 0.10 wt%. The difference in Al, Na and Mg between zones of maximum contrast is ≤1 wt% Al<sub>2</sub>O<sub>3</sub> (max. 0.07 Al cpfu), and ≤0.5 wt% Na<sub>2</sub>O and MgO each. Vanadium and Cr, which result in the typical emerald colour (Schwarz and Schmetzer, 2002), are present in variable, but minor amounts of ≤0.05 wt% (≤0.004 cpfu). Iron is minor, and the average Mg# = Mg/(Mg+Fe) is 0.96, average Cr# = Cr/(Cr+V) is 0.29, similar to the values reported in the overview for emeralds from Colombia (Franz et al., 2020). Caesium, K and Fe contents are minor as reported for Colombian emeralds in the review about trace elements by Saeseaw et al, (2019), and because the dominant incorporation of Cs in beryl occurs via substitution with Li (Aurischio et al., 1988), we infer that Li contents are also minor.

**Table 2.** Composition (EMPA) of beryl crystals; formulae were calculated.

Sample/ analysis	2014-1 01	2014-1 02	2014-2 01	2014-2 02	2014-3 01	2014-3 02	2014-3 03	2014-4 01	2014-4 02	2014-5 01	2014-5 02
<b>Wt%</b>											
SiO <sub>2</sub>	67.26	67.15	66.76	66.77	66.34	66.18	67.44	66.534	66.25	66.98	66.827
TiO <sub>2</sub>	0.004	bdl	0.004	bdl	bdl	0.006	bdl	bdl	0.005	0.001	bdl
Al <sub>2</sub> O <sub>3</sub>	18.21	17.93	18.60	18.02	17.63	17.86	18.61	17.96	17.72	18.07	17.82
Sc <sub>2</sub> O <sub>3</sub>	0.002	0.004	0.015	bdl	bdl	0.013	0.016	0.015	bdl	bdl	bdl
Cr <sub>2</sub> O <sub>3</sub>	0.018	bdl	0.007	0.009	0.006	0.009	bdl	0.042	0.037	0.052	bdl
V <sub>2</sub> O <sub>3</sub>	bdl	0.05	0.039	0.006	0.013	0.036	0.044	0.103	0.04	0.024	0.019

<b>FeO<sub>tot</sub></b>	0.021	0.052	0.019	0.014	0.021	0.043	0.032	0.01	0.021	0.041	0.040
<b>MnO</b>	0.007	0.016	0.006	0.033	0.009	bdl	bdl	0.025	0.001	bdl	bdl
<b>MgO</b>	0.581	0.578	0.095	0.631	0.711	0.615	0.26	0.51	0.744	0.649	0.595
<b>CaO</b>	0.008	bdl	0.008	0.009	0.008	bdl	0.002	0.021	bdl	bdl	bdl
<b>Na<sub>2</sub>O</b>	0.475	0.452	0.089	0.49	0.598	0.498	0.200	0.419	0.634	0.502	0.481
<b>K<sub>2</sub>O</b>	0.002	0.016	0.013	0.007	0.016	bdl	0.013	0.005	0.013	0.013	0.008
<b>Cs<sub>2</sub>O</b>	0.010	0.001	0.018	bdl	bdl	bdl	0.004	0.025	bdl	bdl	0.009
<b>BeO<sub>calc</sub></b> *	13.99	13.93	13.88	13.89	13.78	13.77	14.02	13.84	13.79	13.94	13.86
<b>Total</b>	100.59	100.18	99.55	99.87	99.14	99.03	100.63	99.53	99.25	100.29	99.66
<b>cpfu**</b>	on the basis of 18 oxygen										
<b>Si</b>	6.002	6.017	6.006	6.002	6.011	6.001	6.005	6.003	5.999	5.998	6.018
<b>Al</b>	1.914	1.892	1.971	1.908	1.882	1.907	1.952	1.911	1.890	1.908	1.890
<b>Sc</b>	-	-	0.001	-	-	0.001	0.001	0.001	-	-	-
<b>Cr</b>	0.001	-	-	0.001	-	0.001	-	0.003	0.003	0.004	-
<b>V</b>	-	0.004	0.003	0.000	0.001	0.003	0.003	0.007	0.003	0.002	0.001
<b>Fe<sup>2+</sup></b>	0.002	0.004	0.001	0.001	0.002	0.003	0.002	0.001	0.002	0.003	0.003
<b>Mn<sup>2+</sup></b>	0.001	0.001	-	0.003	0.001	-	-	0.002	-	-	-
<b>Mg</b>	0.077	0.077	0.013	0.085	0.096	0.083	0.035	0.069	0.100	0.087	0.080
<b>Ca</b>	0.001	-	0.001	0.001	0.001	-	-	0.002	-	-	-
<b>Na</b>	0.082	0.079	0.016	0.085	0.105	0.088	0.035	0.073	0.111	0.087	0.084
<b>K</b>	0.000	0.002	0.001	0.001	0.002	-	0.001	0.001	0.002	0.001	0.001
<b>Be</b>	3.000	3.000	3.000	3.000	3.000	3.000	3.000	3.000	3.000	3.000	3.000
<b>total cations</b>	11.081	11.075	11.015	11.086	11.101	11.087	11.035	11.073	11.110	11.090	11.078
<b>sum oct</b>	1.995	1.978	1.990	1.997	1.982	1.998	1.993	1.994	1.998	2.003	1.975
<b>Mg/(Mg+Fe)</b>	0.98	0.95	0.90	0.99	0.98	0.96	0.94	0.99	0.98	0.97	0.96
<b>Cr/(Cr+V)</b>	1.00	0.00	0.15	0.60	0.31	0.20	0.00	0.29	0.48	0.68	0.00

bdl = below detection limit; \*calculated for Be = 3.000 cations per formula unit; \*\*minor amounts of Ti, Cs neglected



### 3.3 Morphology of the faces

#### 3.3.1 (0001)

The SEM images of the (0001) faces of all crystals shows flat areas and irregular indentations (Fig. 2); the rim of the crystals is mostly complete. Indentations are of variable diameter (in the order of 40–300  $\mu\text{m}$ ) and depth (up to approximately 100  $\mu\text{m}$ ). Most indentations do not follow the symmetry of the crystal and appear irregular (Fig. 2c). Closer inspection, however, reveals partially straight outlines (Fig. 2d), though a complete hexagonal shape is rarely observed. Many indentations are filled with crystals, or the bottom of these indentations are lined with various minerals, which were identified by EDS as dolomite, halite, ZnS, Na-Ca-Mg-Al-silicates, and organic matter (OM, with some N and S); identification was challenging due to charge accumulation in the deeper cavities. Indentations show steeply inclined, wedge-shaped faces inwards (arrows, Fig. 2d), or vertical, negative prism faces, and then a flat bottom.

The shape of the indentations is also visible in BSE images of thin sections cut parallel to the *c*- and *a*-axes of the beryls (Fig. 3). The surface is irregular (Fig. 3a) or has approximately uniform height (Fig. 3b); indentations can have a flat bottom or terminate at obliquely oriented faces (Fig. 3 e–h). They can extend into the interior, where voids, appearing as crack-like features, can also be observed (Fig. 3c).

The flat and smooth appearing surface of (0001) shows multiple growth steps with the characteristic 120° angle for hexagonal symmetry. Step height is variable, with single steps being less than 1  $\mu\text{m}$  estimated from the images (Figs 2e, h). At the apex of the inner 120° angle an EP is observed, whereas no EP is present at the outer 120° angle of the growth steps (Fig. 2e).

The EP are 1–2  $\mu\text{m}$  in diameter (Fig. 2g, h) and are irregularly distributed on the flat (0001) surface (Fig. 2c, d) or aligned (Fig. 2h) and are also seen on the inclined inward faces of large indentations (Figs 2d, f). The EP are P-type (with a pointed bottom) with a star-shaped pattern (Fig. 2g) at the bottom, which is not clearly visible in EP with steeply inclined faces. Hexagonal outline of the round appearing EP is in many examples only poorly developed (Fig. 2h).



**Figure 2.** SEM images, with SE(L) detector, (a) and (b) in LM(L) mode, of (0001), crystals #1, 2, and 3. (a, b) Overview, illustrating the irregular shape of indentations. White rectangles indicate position of details in (c, d). (c) Indentations partly show a flat bottom, some are filled with minerals. (d) Indentations show small faces, pointing inwards (arrows). (e) Growth steps on (0001) with a  $120^\circ$  angle, which are decorated with EP (arrows). EP also occur on the flat parts and (f) within the large

indentations. (g) EP with the characteristic hexagonal outline, (h) which can also be aligned in chains; arrows point to growths steps.

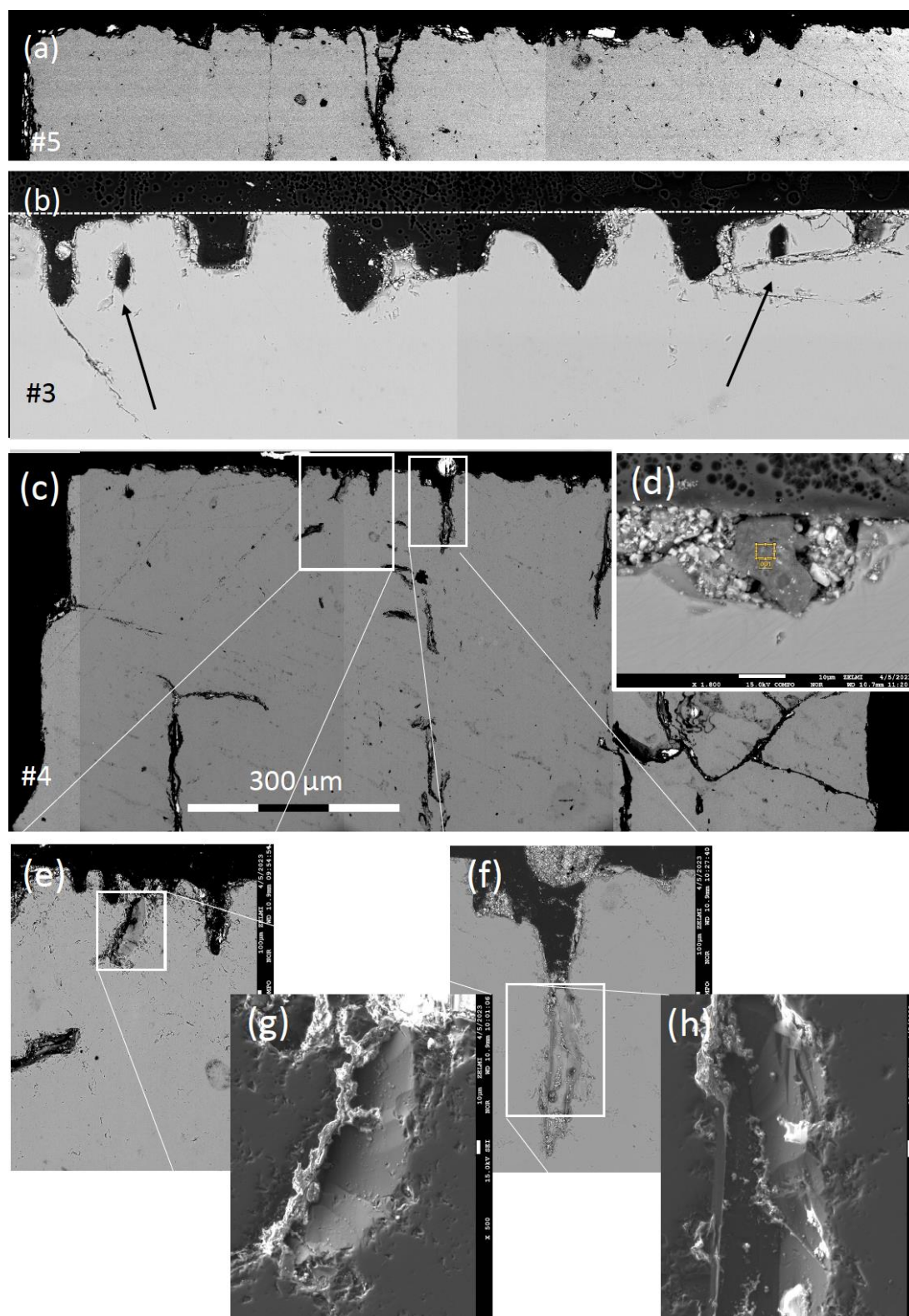


**Figure 3.** BSE images of upper part of crystals #3, 4 and 5, *c*-axis oriented vertical, *a*-axis horizontal. (a) The trace of (0001) is irregular, (b) and has approximately the same height (dotted line); indentations can have a flat bottom or are ending on obliquely oriented faces; arrows point to cavities, which are closed in the upper part. (c) Indentations can continue into the interior, where

also crack-like features can be seen. (d) Indentations are partly filled with crystals (white contrast) and with organic matter (centre, dark contrast, yellow frame). (e, f) Details of indentations, with corresponding secondary electron images (SEI detector) (g, h), showing oblique faces extending into the crystal.

### 3.3.2 Prism faces

The SEM images of  $\{10\bar{1}0\}$  faces (Fig. 4) show isolated EP and EP chains; chains are of different length with just a few EP or up to several tens of EP (Fig. 4a). The chains are oriented parallel to  $c$ , but there are also slight deviations  $\leq 6^\circ$  from  $c$ . The close and regular spacing of 1.5–2  $\mu\text{m}$  between individual EP in chains is characteristic, coalescing to an etching channel (Fig. 4b). The EP are both P-type and F-type (with a flat bottom) (Fig. 4c). EP chains can also be oriented oblique to the  $c$ -axis in various angles. These EP are predominantly F-type and also occur as isolated etch pits (Fig. 4d). On a different  $\{10\bar{1}0\}$  face of the same crystal (crystal #2 Fig. 4e, f), the angle of three EP chains towards the  $c$ -axis varies from a few degrees to strongly oblique. In one case, EP chains that were crossing the border towards the second order prism (Fig. 4g) with growth steps were observed. Some of the EP are strongly elongated parallel to the crystals  $a$ -axis, and with a pointed bottom (Fig. 4h).

The second-order prism  $\{11\bar{2}0\}$  is developed in three of the investigated crystals (Fig. 5). The faces are much smaller than the first-order prisms, are not present on each side of a crystal, and they show a completely different morphology compared to the first-order prisms. Etch pits are absent or rare; instead, the faces are characterized by what we interpret as growth structures. These structures are wedge-shaped, anastomosing grooves, which extend over several hundreds of  $\mu\text{m}$ , subparallel to the  $c$ -axis (Fig. 5b, e, f), and can have a flat bottom (Fig. 5c). The grooves are created by curved growth steps on the adjacent first-order prisms. Within these grooves, small asymmetric F-type EP are rarely found (Fig. 5d), arranged in a chain subparallel to the grooves. The wedge-shaped features are orientated in the same direction (Fig. 5g). On the flat area, there are approximately 10  $\mu\text{m}$  wide grooves, elongated parallel to the  $c$ -axis (Fig. 5h).

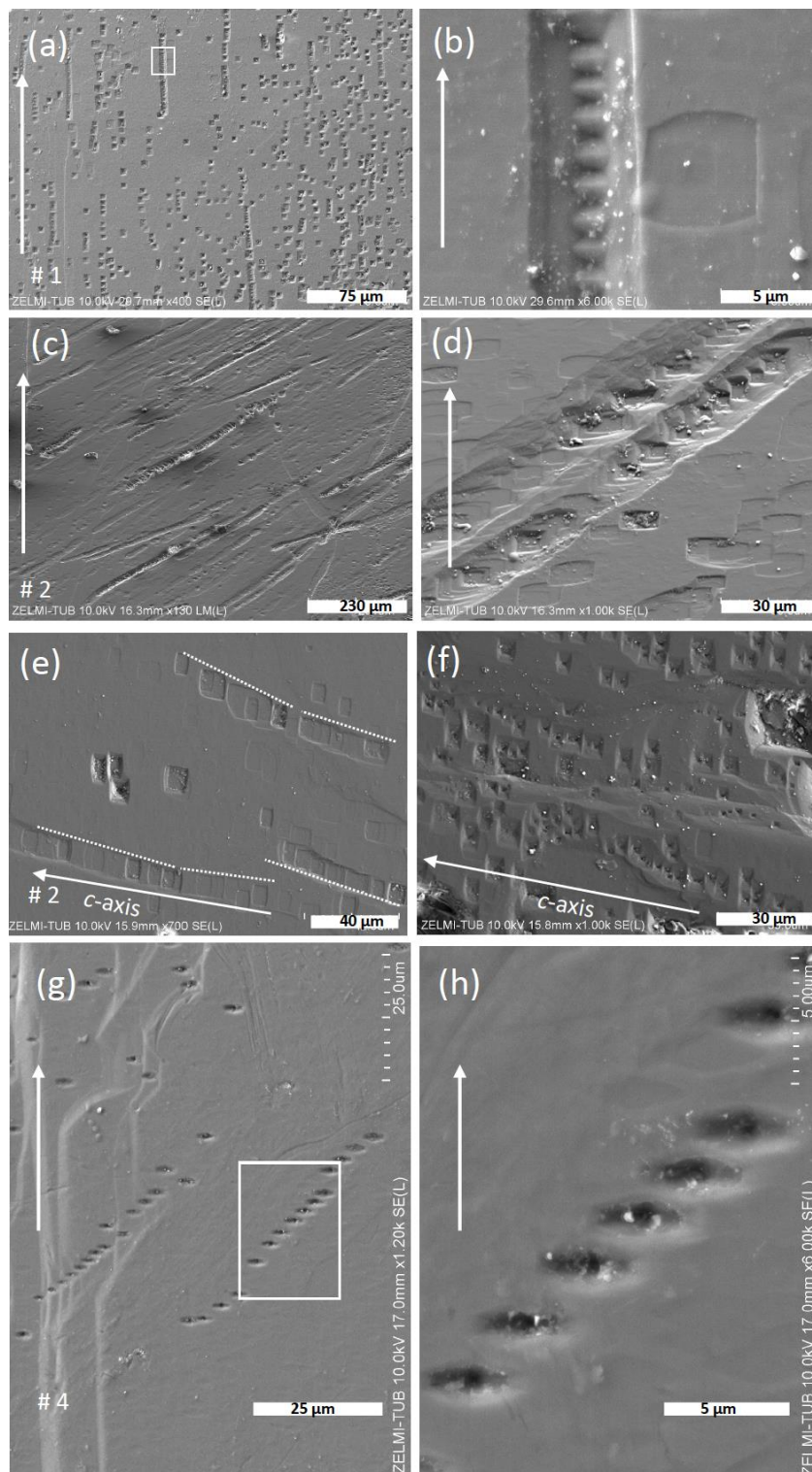




**Figure 4.** SEM images with SE(L) detector of first-order prism  $\{10\bar{1}0\}$ ;  $c$ -axis is oriented parallel to white arrow. (a) EP are aligned in chains of different length, but occur also isolated. The chains are oriented parallel to  $c$ , but note also deviations from  $c$ . White rectangle shows position of (b), close and regular spacing between individual EP, coalescing to an etching channel. (c) EP chains, oriented oblique to  $c$  in various angles. (d) Detail of the same face of two parallel oriented chains, strongly oblique to  $c$ ; EP are dominantly F-type and occur also isolated. (e) F-type EP chain on a different  $\{10\bar{1}0\}$  face of the same crystal # 2; variable orientation of the chains is indicated by dotted lines. (f) Irregularly oriented chains of P-type EP. (g) EP chains, crossing the border to the second order prism with growth steps (left part of the image between labels 'g' and '# 4'; white rectangle indicates position of (h), showing EP strongly elongated parallel to the  $a$ -axis, and with a pointed bottom.

Prepublished article

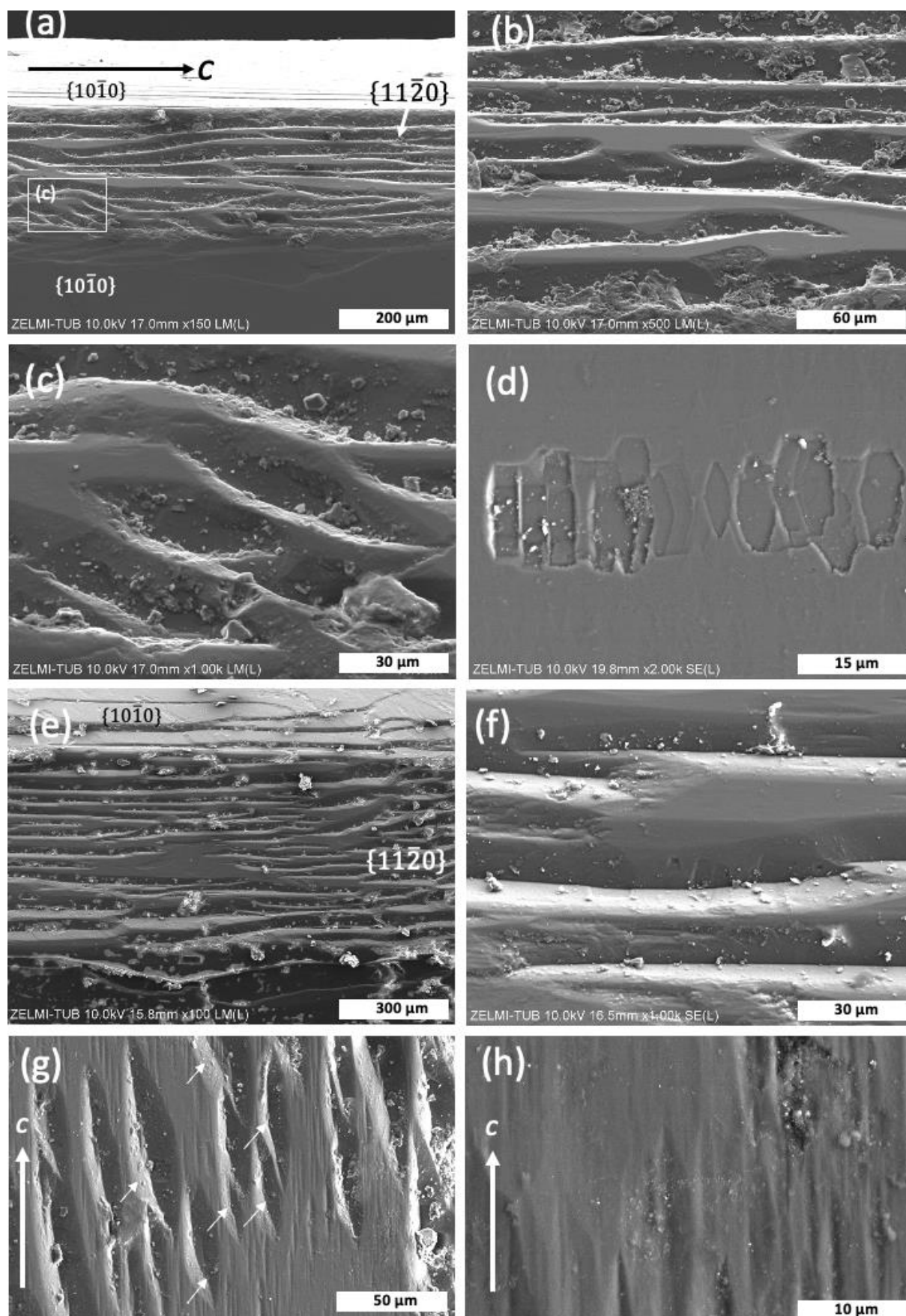


**Figure 5.** SEM images of second-order prism  $\{11\bar{2}0\}$ . (a) The second-order prism occurs between two first-order prisms above and below ( $c$ -axis is oriented horizontal). The face consists of flat areas and

anastomosing wedge-shaped features, shown enlarged in (b). White rectangle indicates position of (c), illustrating the subparallel oriented wedge-shaped features. (d) Detail of a flat part of the second-order prism with a chain of F-type EP, elongated in direction of the  $a$ -axis. (e, f) Second-order prism of crystal #4, showing similar features as in crystal #2. (g) Second-order prism of crystal #1 ( $c$ -axis oriented vertical), showing the wedge-shaped features with similar orientation (arrows). (h) Detail of (g), showing a flat area with approximately 10  $\mu\text{m}$  wide grooves, elongated parallel to  $c$ . (e) and (f) with SE(L) detector, all others in LM(L) mode.

### 3.3.3 Conical growth

Crystal #5 shows conical growth on one side of the crystal (Fig. 6a, b), approximately 200  $\mu\text{m}$  wide and characterized by horizontal stripes. Closer inspection shows that the stripes are undulating ridges and valleys, subparallel to the  $a$ -axis (Fig. 6c, d); they are approximately 10 to 20  $\mu\text{m}$  wide (Fig. 6e). In cross-section, the transition from the lower part of the first-order prism to the upper part is marked by a smooth, continuous curvature (Fig. 6f).



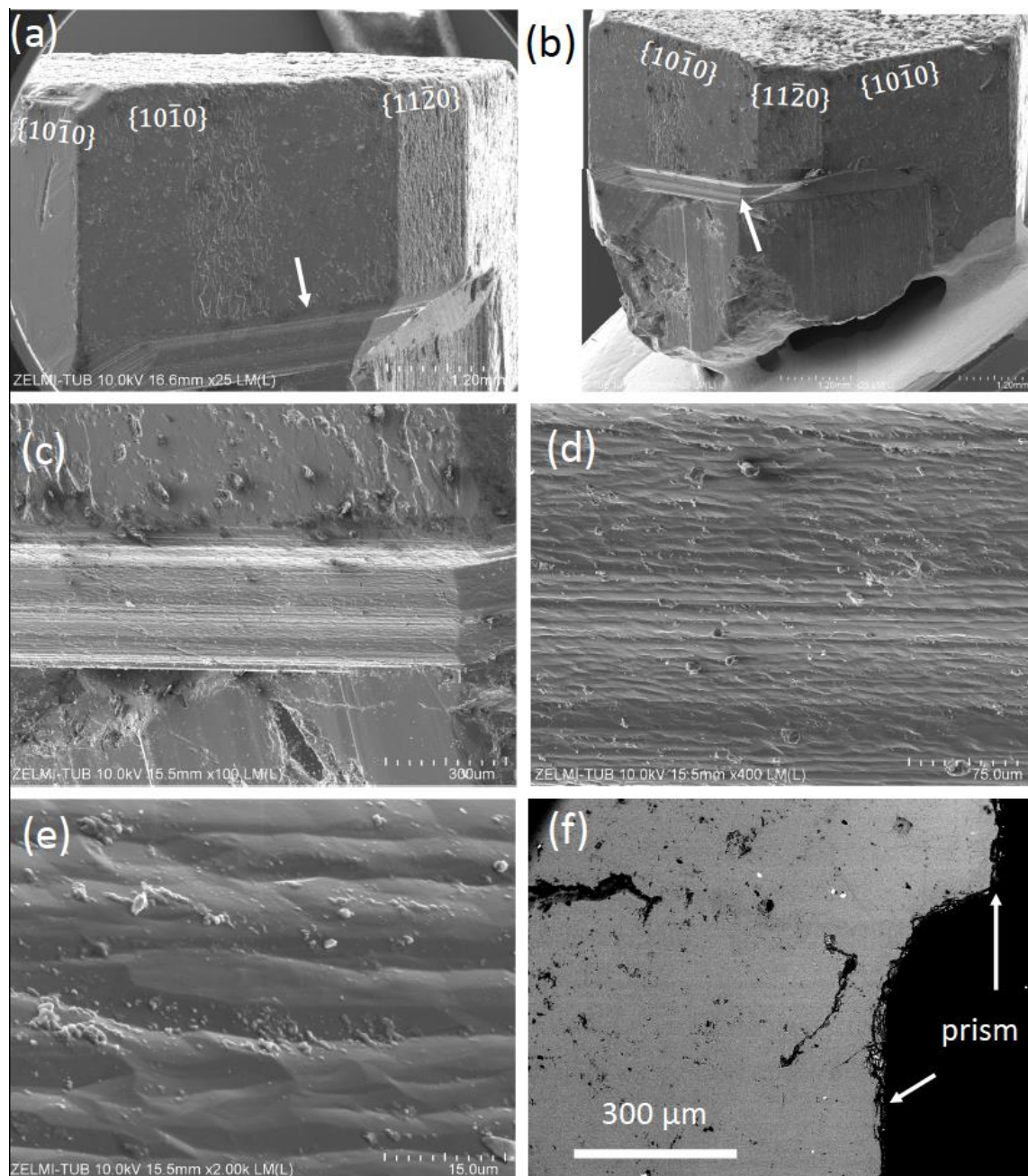


**Figure 6.** SEM images (LM(L) mode) of crystal #5 (a-e), and BSE image (f) illustrating conical growth. (a, b) Overview of the crystal with first- and second-order prisms and conical area (arrow). (c, d) Striped surface of the transition from the lower to the upper part of the prism face. (e) Detail, showing undulating ridges and valleys. (f) Cross section, showing a smooth curvature at the transition.

### 3.4 Interior features – chemical zoning

All crystals exhibit sector zoning with *c*- and *a*-sectors (or pinacoid- and prism sectors), and the different phenomena of the sector zoning are schematically depicted in Fig. 7. Zoning was investigated with  $\mu$ XRF element distribution maps (Fig. 8). They are semi-quantitative only, and due

to the varying fluorescence yield of elements, no direct information on absolute amounts can be obtained. We distinguish between straight and curved (convex/concave) sector boundaries, and within sectors, we observed stripes parallel and oblique to the *c*-axis and growth bands parallel to the *a*-axis. The sector boundaries can be irregular, here described as serrate. Based on the sector zoning with lesser truncation of the *c*-sector, it can be inferred that crystals #1, 2, and 3 are the most complete. Crystal #5 shows a small conical growth (similar to a sceptre) on one side of the crystal.

In all crystals, the *c*-sector is enriched in Na and Mg (Fig. 9), whereas the *a*-sector is enriched in Al, V, Fe and Cr. Sector boundaries as they show up for different elements are straight for V and Fe in crystal #5, concave in crystal #1, convex for Cr in crystal #3, serrate and incomplete for V in crystal #3, but straight and extending further towards the root zone in this crystal. Growth bands are only seen for V and Fe in the *c*-sectors. Crystal #4 (the most intensely coloured crystal) shows the strongest V-intensities in the outermost rim of the *a*-sector, parallel with Cr. Stripes with relative enrichment/depletion of elements parallel to the crystal's *c*-axis are an artefact of X-ray diffraction in  $\mu$ XRF spectra.

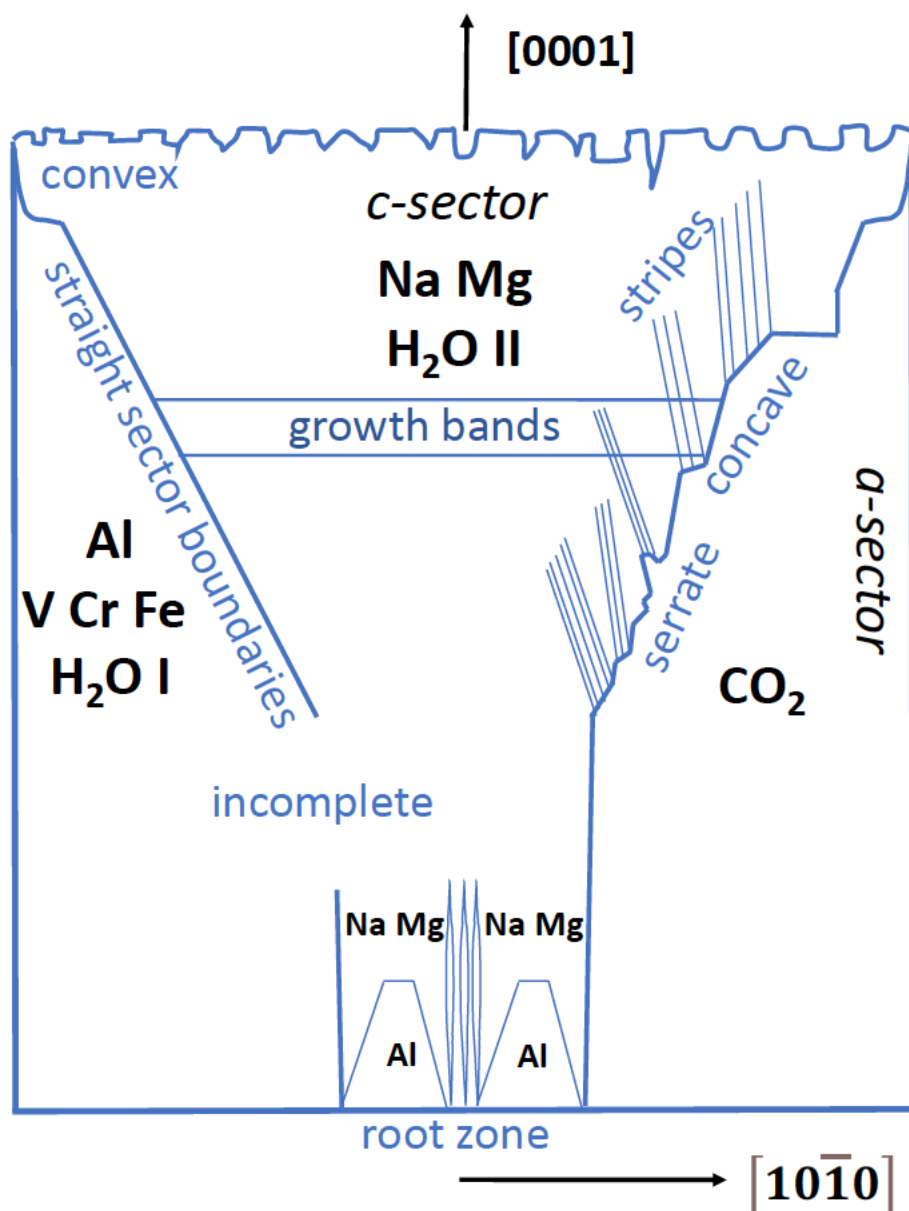


**Figure 7.** Schematic zoning patterns and summary of results of Colombian beryls, in cross sections parallel to the crystals'  $[1000]$  and  $[10\bar{1}0]$  directions. Crystals grew onto a substrate from a root zone in one direction. Sector boundaries can be straight, convex/concave curved, or serrate, and sectors can be incomplete. The  $c$ -sectors show zones called growth bands. The  $a$ -sectors are enriched in V, Cr, Fe and H<sub>2</sub>O I and CO<sub>2</sub>, the  $c$ -sectors in Na, Mg (arranged in stripes) and H<sub>2</sub>O II. The root zone shows enrichment of Al in hillocks and stripes, which disappear with further growth in  $[1000]$ .

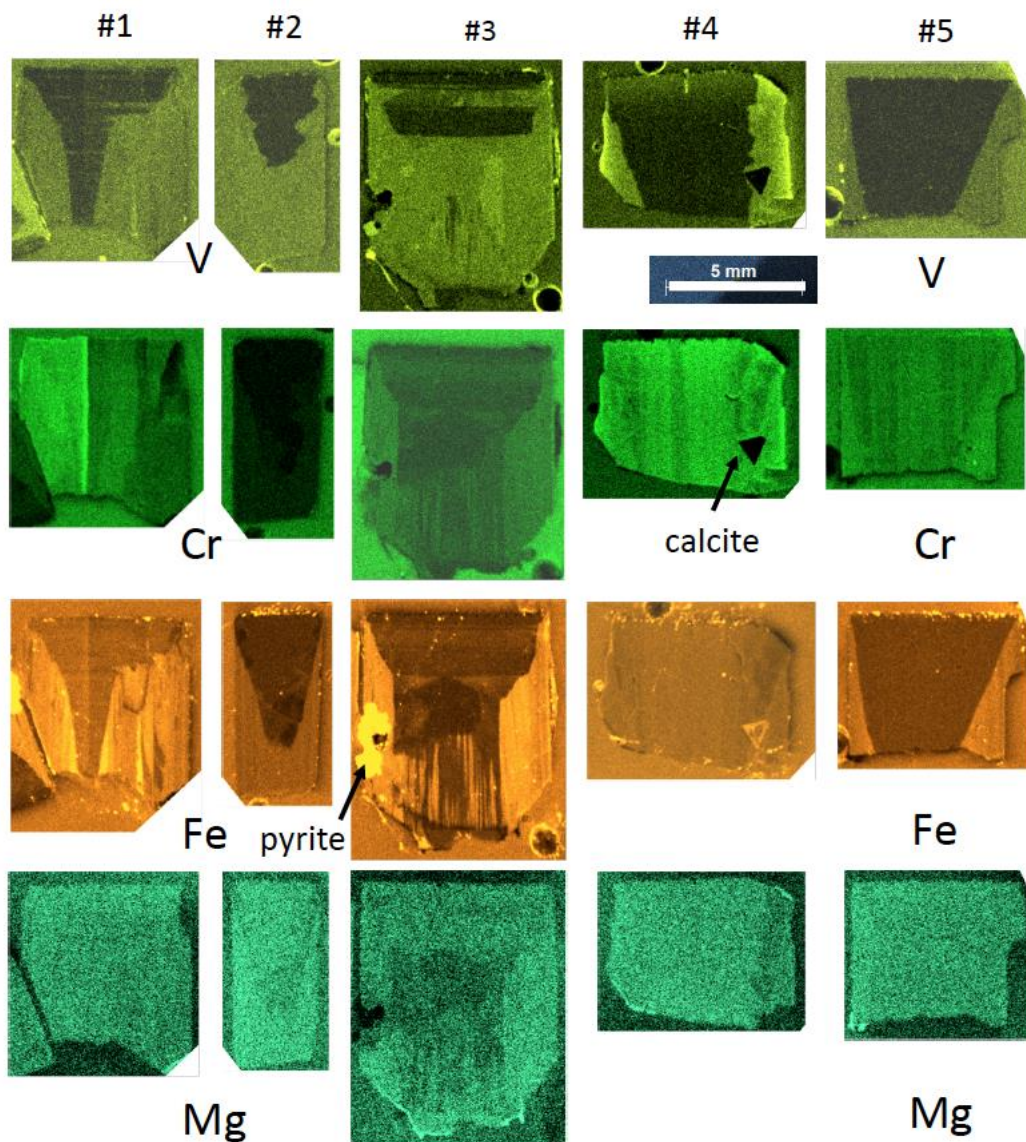


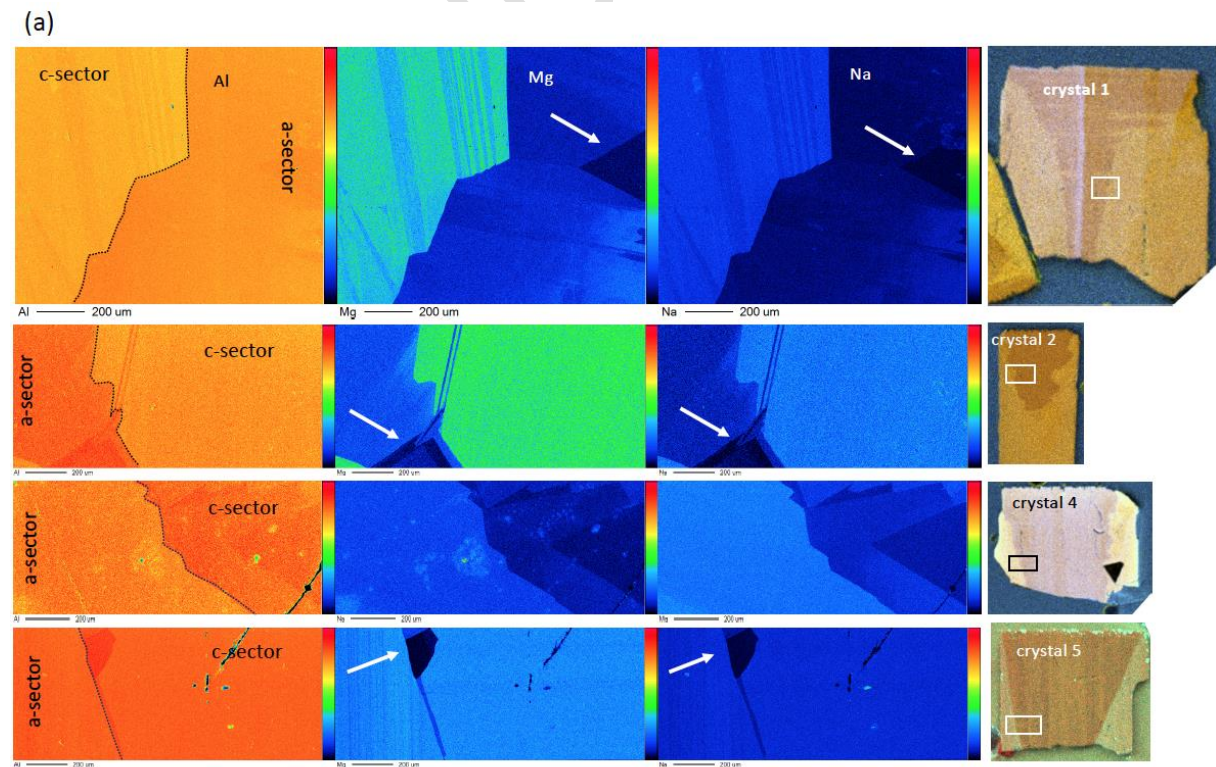
**Figure 8.** Element distributions for V, Cr, Fe and Mg, determined by  $\mu$ XRF. All crystals show sector zoning. A root zone is seen in crystal #3. Crystals #3 and 4 contain large inclusions of pyrite (#3) and calcite (#4). Stripes with apparent elemental variation parallel to the c-axis result from orientation-dependent diffraction, falsely quantified by the  $\mu$ XRF software as changes in elemental concentration. For detailed description see text.

From the overview of the zoning pattern, as seen in the  $\mu$ XRF data, we selected areas for a more detailed mapping by EMPA (Fig. 9), focussing on the sector boundaries, in crystal #3 on the top zone with indentations, and on the root zone. While Mg- and Al zoning is hardly visible in the  $\mu$ XRF maps, they are most pronounced in EMPA. Mg and Na are enriched in areas where Al is relatively low, indicating the substitution  $^{VI}\text{Mg}^{+\text{channel}}\text{Na} = ^{VI}\text{Al}^{+\text{channel}}\square$ . Some areas with a triangular outline seem to be nearly devoid of Mg+Na (marked by arrows in Fig. 9a). A common feature is that what appears as straight or serrate boundaries is, in fact, a stepped boundary, with steps ranging from tens to



approximately hundred  $\mu\text{m}$ . Stripes associated with the (Mg+Na)-substitution in the *c*-sector are parallel, but inclined to the *c*-axis by variable angles. The steps in the sector boundary are straight lines, but do not follow an obvious crystallographic direction with low Miller's indices. The upper 200  $\mu\text{m}$  (measured in crystal #3) are homogeneous, indicating that the indentations on (0001) do not show up in the zoning of Al, Na and Mg. However, below this zone the *c*-sector shows a complicated pattern with zones very poor in Mg+Na.

Crystal #3, which shows a root zone (Fig. 9b), started to grow in its central part homogeneously, rich in Al, poor in Mg, Fe, Cr and V (Figs. 7, 9). Note, however, that the imaging is 2D, and for a complete picture of the growth features, sections showing the element distribution in the root zone perpendicular to the *c*-axis would be necessary. Where the *a*-sectors evolved to the right and left, these sectors are enriched in Fe, Cr and V. The detail of this EMPA mapping (Fig. 10) shows the root zone, with Mg-poor/Al-rich hillocks of up to 100  $\mu\text{m}$  wide and high, forming a bridge-like feature. From these hillocks irregular formed stripes extend in [0001], but not strictly parallel to the *c*-axis. With further growth in *c*-direction, Mg-enrichment suddenly begins at a certain point, continuing upwards and eventually pinching out after several 100  $\mu\text{m}$  of growth. In the upper part of the mapped area, irregular zones appear, which are either depleted (left circle in Fig. 10) or enriched in Mg (right circle).



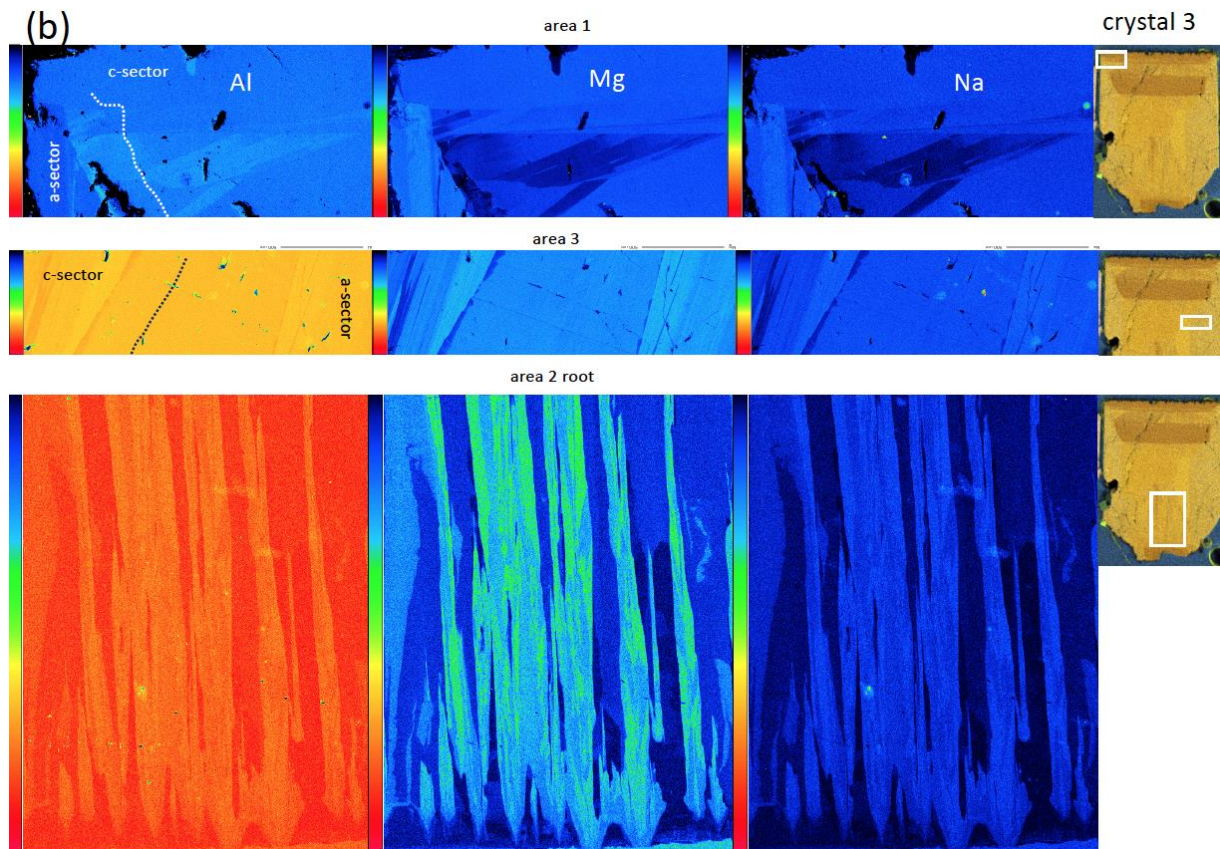


**Figure 9a,b.** Element distribution maps obtained by EMPA of Al, Mg and Na for selected areas (a) in crystals #1, 2, 4 and 5, (b) in crystal #3. Position of the mappings is indicated by white rectangles in the  $\mu$ XRF mapping for Al. The sector boundaries (outlined) are stepped and show a characteristic stripe pattern with low Mg, Na contents; arrows point to specific areas, rich in Al, and with Mg and Na below detection. In crystal #3, area 1 shows the homogeneous upper part with an indentation (black in Mg-Na map, partly filled with an Al-rich mineral), and below this homogeneous part a very complicated pattern of Mg+Na substitution; area 3 shows the sector boundary with the characteristic stripe pattern; area 2 the root zone with Al-rich hillocks and stripes of Mg+Na enrichment.



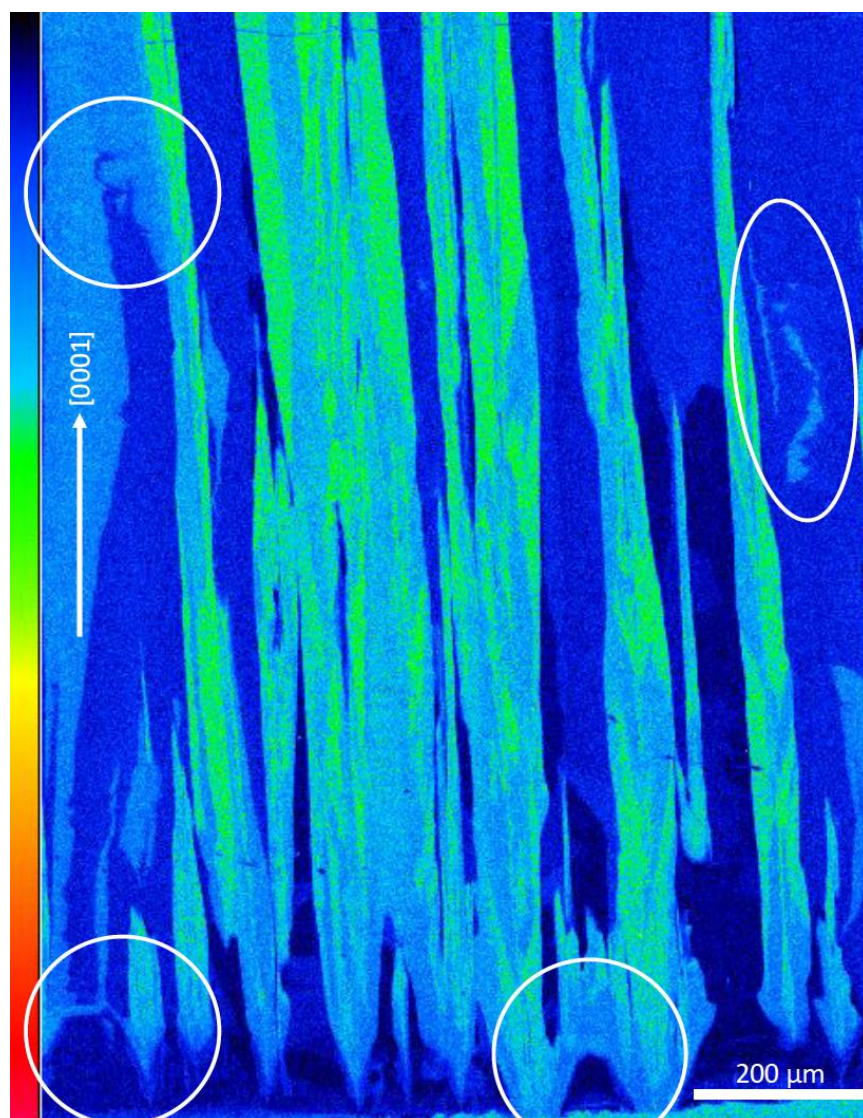


**Figure 10.** Mg distribution in the root zone of crystal # 3. Areas with special features are encircled: the lower two circles indicate growth zones, poor in Mg, with the beginning of *c*-sectors enriched in Mg, the upper two circles indicate irregular areas enriched/depleted in Mg. Note the variable shape of the Mg-enriched stripes, subparallel to the *c*-direction

### 3.5 IR spectroscopy

A summary of all observed main vibrational bands and combined vibration-rotation frequencies of trapped molecules in beryl structural channels is given in Table 3. The polarized IR spectra of the oriented samples show the presence of both types of H<sub>2</sub>O molecules in the channels, type I with the H-H vector parallel to the crystal's *c*-axis, and type II, with the H-H vector parallel to the *a*-axis (Table 3). The presence of two structural types of water molecules with differing bond strength prevents the quantification of H<sub>2</sub>O content, as can be performed in glasses or for OH<sup>-</sup> groups in minerals (e.g.

Libowitzky and Rossman, 1997). Each of them gives rise to several bands in two different polarizations and at least some of these bands ( $\nu_1$  of H<sub>2</sub>O I) are not linearly dependent on concentration. Additionally, molecules H<sub>2</sub>O I cause strong liberation side-bands, whereas H<sub>2</sub>O II does not. Thus, we rely on semi-quantitative assessment of the amounts of each type of water separately, as well as on the H<sub>2</sub>O I/H<sub>2</sub>O II ratios in different samples or zones of crystals, rather than determining the exact amount of water. Representative spectra of crystals #1 and 3 are shown in Fig. 11 (for complete set see supplementary material). In the E ||  $\alpha$  polarized IR spectra of the H<sub>2</sub>O stretch bands area, the broad band at 3660 cm<sup>-1</sup> results from the H<sub>2</sub>O II antisymmetric stretch vibrations (Table 3). The *c*-sector is enriched in H<sub>2</sub>O II. Comparison of combined  $\nu_2+\nu_3$  bands of H<sub>2</sub>O I and H<sub>2</sub>O II in the  $\alpha$ - and *c*-sectors show that the *c*-sector is slightly enriched in H<sub>2</sub>O II, but depleted in H<sub>2</sub>O I.

CO<sub>2</sub> molecules are also present, but to a minor extent (Fig. 11c). The polarized IR spectra with E ||  $\alpha$  of the CO<sub>2</sub>  $\nu_3$  band area in different sectors indicate that the  $\alpha$ -sector is enriched in CO<sub>2</sub>. In both sectors CO<sub>2</sub> concentration decreases from the central part to the rims. Because cordierite is isostructural with beryl, and the orientation of the linear CO<sub>2</sub> is perpendicular to the *c*-axis in cordierite (Khomenko and Langer, 2005), we assume the same orientation in beryl.



**Table 3.** Summary of main vibrational bands and combined vibration-rotation frequencies ( $\text{cm}^{-1}$ ) of trapped molecules in beryl structural channels. Polarization is given relative to crystal's *c*-axis as perpendicular  $\perp$  and parallel  $\parallel$ .

Assignment				Free	Type I	Type II	Free	Channel $\text{CO}_2$ ( $\nu_3$ ) $\perp$		
$\nu_1$	$\nu_2$	$\nu_3$	$\nu_4$	$\text{H}_2\text{O}^{(1)}$	$\text{H}_2\text{O}$	$\text{H}_2\text{O}$	$^{12}\text{CO}_2^{(1)}$	$^{12}\text{CO}_2$	$^{13}\text{CO}_2$	
0	1	0	$-l_1$	1545 <sup>2)</sup>	$\perp$					
0	1	0		1595	1595 <sup>2)</sup> -1600 <sup>3)</sup>	$\perp$	1628 <sup>2)</sup> -1632 <sup>3)</sup>	$\parallel$		
0	1	0	$+l_1$	1645 <sup>2)</sup>	$\perp$					
1	0	0		3652	3600-3607 <sup>3)</sup>	$\perp$	3592 <sup>2)</sup> -3596 <sup>3)</sup>	$\parallel$		
0	0	1	$-l_2$	3521 <sup>2)</sup>	$\perp$				2339 <sup>2)</sup>	
0	0	1		3756	3694 <sup>2)</sup>	$\parallel$	3655-3660 <sup>3)</sup>	$\perp$	2349	2354 <sup>2)</sup> -2360 <sup>3)</sup>
0	0	1	$+l_2$	3860 <sup>2)</sup>	$\perp$				2369 <sup>2)</sup>	2289-2290 <sup>3)</sup>
0	1	1	$-l_2$	5107 <sup>2)</sup>	$\perp$	4958 <sup>2)</sup>	$\parallel$			
0	1	1		5335	5273 <sup>2)</sup> -5277 <sup>2)</sup>	$\parallel$	5271 <sup>2)</sup>	$\perp$		
0	1	1	$+l_2$	5455 <sup>2)</sup>	$\perp$	5593 <sup>2)</sup>	$\parallel$			
0	2	1		6874	6821 <sup>2)</sup>	$\parallel$	6849 <sup>2)</sup>	$\perp$		

\* symmetric stretching, \*\* bending, \*\*\* antisymmetric stretching vibrations, \*\*\*\* side bands due to liberation motion; References: <sup>1)</sup> Herzberg (1945) <sup>2)</sup> Wood and Nassau (1967); <sup>3)</sup> this study

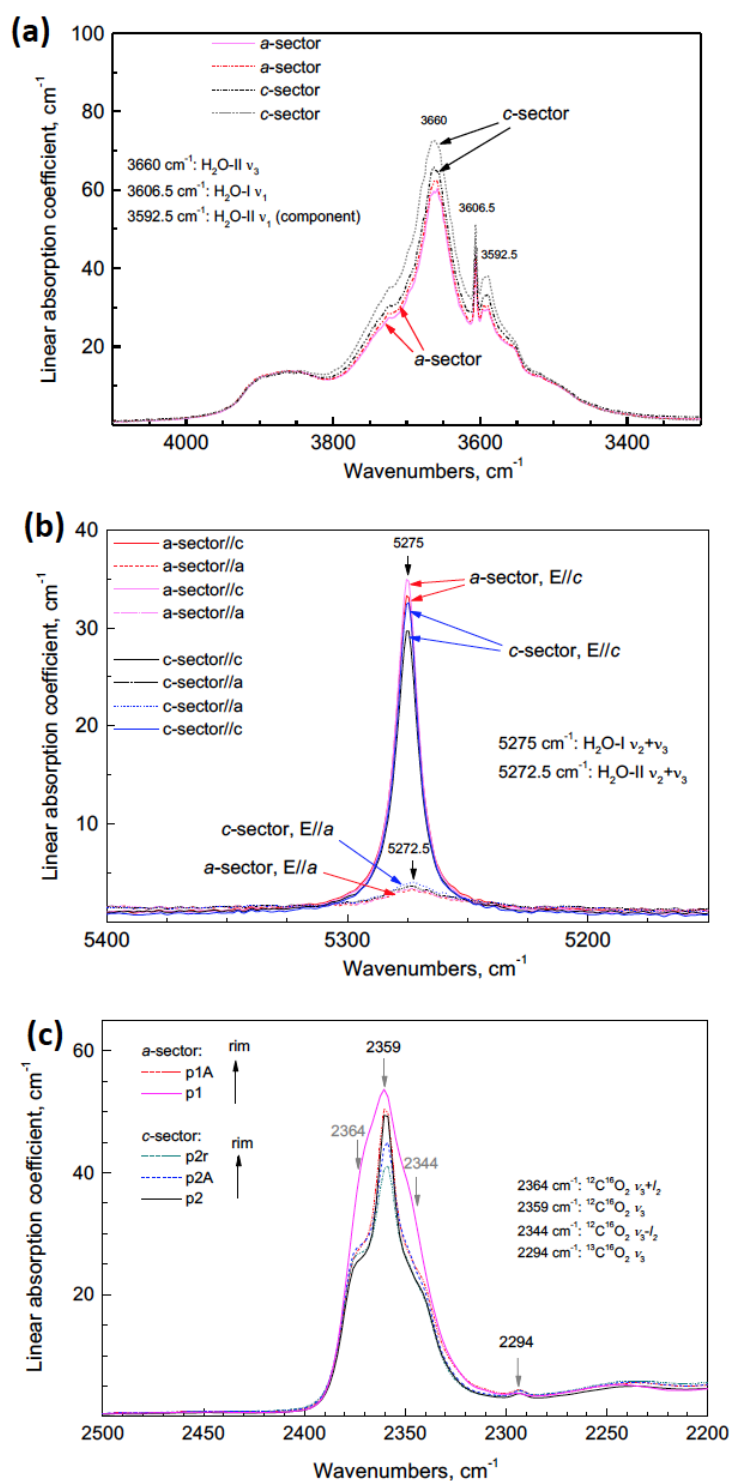


**Figure 11.** (a) Polarized IR spectra E||a of the H<sub>2</sub>O stretching bands area of crystal # 1. Broad band at 3660 cm<sup>-1</sup> is due to H<sub>2</sub>O II (H-H vector perpendicular to the a-axis) antisymmetric stretching vibrations. The c-sector is enriched in H<sub>2</sub>O II, as it is also slightly enriched in Na (+Mg) (see Fig. 9). (b) Comparison of combined v<sub>2</sub>+v<sub>3</sub> bands of H<sub>2</sub>O I (H-H vector parallel to c-axis) and H<sub>2</sub>O II in different sectors. The c-sector is slightly enriched in H<sub>2</sub>O II, but depleted in H<sub>2</sub>O I. (c) Polarized IR spectra E||a of the CO<sub>2</sub> v<sub>3</sub> band area of crystal no. 3 in different sectors. The a-sector is enriched in CO<sub>2</sub>. In both sectors CO<sub>2</sub> concentration decreases clearly from the central part to the rims.

## 4 Discussion

### 4.1 Growth

Growth features on (0001) appear as growth steps (Fig. 2e, h). The  $120^\circ$  angle of the steps indicates that they result from growth along screw dislocations. Other growth features on (0001) (Fig. 2a, b) are the indentations, especially when combined with cross sections and corresponding BSE images (Fig. 3). The cross sections show that the indentations with a flat bottom or terminating with obliquely oriented faces are of similar depth, forming a palisade-like structure; indentations can extend into the crystals and continue in features which resemble cracks. Closer inspection shows oblique faces (Fig. 3e–h), which rules out their formation as cracks during brittle deformation (or sample preparation) and instead suggests they are a growth feature. Palisade-like structures formed through preferential growth in the *c*-direction, followed by growth in the  $\alpha$ -direction, which led to the forming of cavities by closing the indentations in the upper part. Indentations are partly filled with crystals and with organic matter (Fig. 3d), which might have prevented further growth in *c*-direction. Another argument in favour of a growth feature, rather than a dissolution feature is the shape, which, in the case of dissolution should result in a reversed trumpet form, such as observed in pegmatitic beryls (Bartoshinskiy et al., 1969; Franz et al., 2023; Renfro et al., 2023).

The elevated, continuous rims of (0001) are similar to the *vaso*- or spongy-type emeralds from the Chivor mining district in Colombia, described by Pignatelli et al. (2022) and Schmetzer and Martayan (2023). This rim does not show signs of dissolution; if the indentations on (0001) were formed by dissolution, the crystal edges would typically be the first areas to be attacked (Sunagawa, 2005). A pyramidal face (which corresponds to the corner between (0001), first- and second-order prisms) was only observed in crystal #4 (see supplementary material); it also shows an elevated rim and no signs of dissolution. Additionally, the edge between the first-order- and second-order prisms is characterized by growth steps, and not by dissolution (Fig. 4g).

No growth features were observed on the first-order prism; the faces are flat (except for dissolution features, see below). The second-order prism is, however, entirely different (Fig. 5). Their much smaller size, not well developed on all crystals and on all sides of a crystal, and the wedge-shaped, anastomosing grooves, which extend over several hundreds of  $\mu\text{m}$  subparallel to the *c*-axis (Fig. 5b, e, f), indicate that their morphology was shaped by growth. The relative growth rates in  $[1000]$  and  $[10\bar{1}0]$  determine the presence (and size) or absence of a second-order prism (Fig. 12a). A change in the relative growth rates is likely responsible for producing the observed pattern. The similar phenomenon of a face with ridges and valleys, which we observed on the crystal with conical growth (Fig. 6), is interpreted in the same manner (Fig. 12b) i.e. by repeatedly changing growth rates in the

$a$ - and the  $c$ -direction. The variation of the growth directions in all three dimensions also explains the anastomosing ridges on the second-order prism (Fig. 5a, b). This type of growth differs from sceptre growth described by Pignatelli et al. (2022), which exhibits a second stage of growth as in sceptre quartz. Our observations align with observations made by Schmetzer and Martayan (2023) for conical crystals, which are characterized by what they called macroscopically visible “growth lines” perpendicular to the  $c$ -axis on the prism faces. These lines might be misinterpreted as vicinal faces.

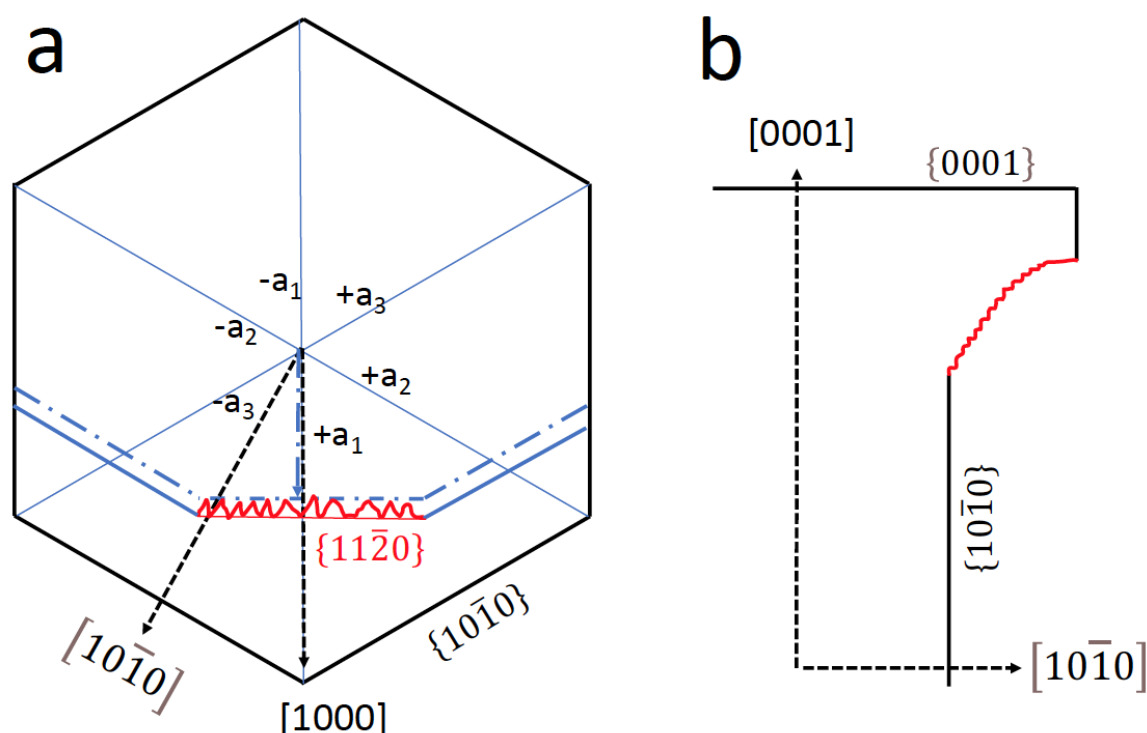


**Figure 12.** Schematic illustration for the formation of (a) the morphology of the second-order prism  $\{11\bar{2}0\}$  and (b) the transition from the lower to the upper part of the conical growth. If growth rate (dashed black arrows) in  $[1000]$  is higher than in  $[10\bar{1}0]$ , no second-order prism develops; if it is lower (blue arrow) it develops. Changes in the relative growth rates produces a morphology with ridges in  $c$ -direction (red line). An analogous change in the growth directions  $[1000]$  and  $[0001]$  produces a similar feature on the conical part of the crystal.

Comparison with experimentally grown beryl in hydrothermal solutions (Demianets et al., 2006) shows that all three commonly developed faces (pinacoids, first- and second-order prisms) grow by a dislocation-mediated layer-by-layer mode, consistent with our observations. The second-order prism shows a higher roughness than the first-order prism, which could also be observed in the natural crystals of this study. However, the growth hillocks, step height and step width, as well as the surface

roughness of the synthetic crystals are in the order of a few nm, whereas on the natural crystals we observe these features on the  $\mu\text{m}$  scale.

## 4.2 Dissolution

Etch pits are observed in many types and occurrences of beryl (Schmetzer and Martayan, 2023). The abundant EP on (0001) (Fig. 2e–h) as well as on the first-order prism (Fig. 4), indicate a high density of defects on these planes; on the second-order prism they are rare (Fig. 5d). The fact that EP also overprint the growth features (Figs 2f, 4g) allows distinguishing between growth and dissolution. Growth steps on (0001) of a few  $\mu\text{m}$  height are also overprinted by EP, typically in the inner  $120^\circ$  angle (Fig. 2e, h), indicating screw dislocations, which later act as initiation sites of dissolution. The different outlines of the 5–10  $\mu\text{m}$  wide P- and F-type EP on the first-order prism (Fig. 13) shows that they are square or mostly elongated perpendicular to the *c*-axis, but also parallel to it, and typically appear with slightly curved outlines, indicating similar dissolution rates, sometimes slightly changing during dissolution, in both directions.

The EP can be arranged in chains (Fig. 2h), indicating a large number of parallel oriented dislocations, what has not been observed in other beryls (Schmetzer and Martayan, 2023; Franz et al., 2023). Such EP coalescence was also described from albite (Beig and Lüttge, 2006) and significantly increases the effective surface area for further dissolution (Lüttge, 2005). The distance of individual P-type EP in a chain varies from 1.3  $\mu\text{m}$  to 4.4  $\mu\text{m}$ , of F-type EP between 4.6  $\mu\text{m}$  and 7.7  $\mu\text{m}$ . In the case of P-type EP, they probably indicate screw dislocations, which can occur in bundles (Sunagawa, 2005), dominantly in the *c*-direction, but also strongly deviating from *c* in various angles. The occurrence of chains of F-type EP, which are ascribed as due to point defects, requires that point defects are aligned. This could occur along edge dislocations, which are the preferred site for e.g. incorporation of atoms with a different ionic radius.

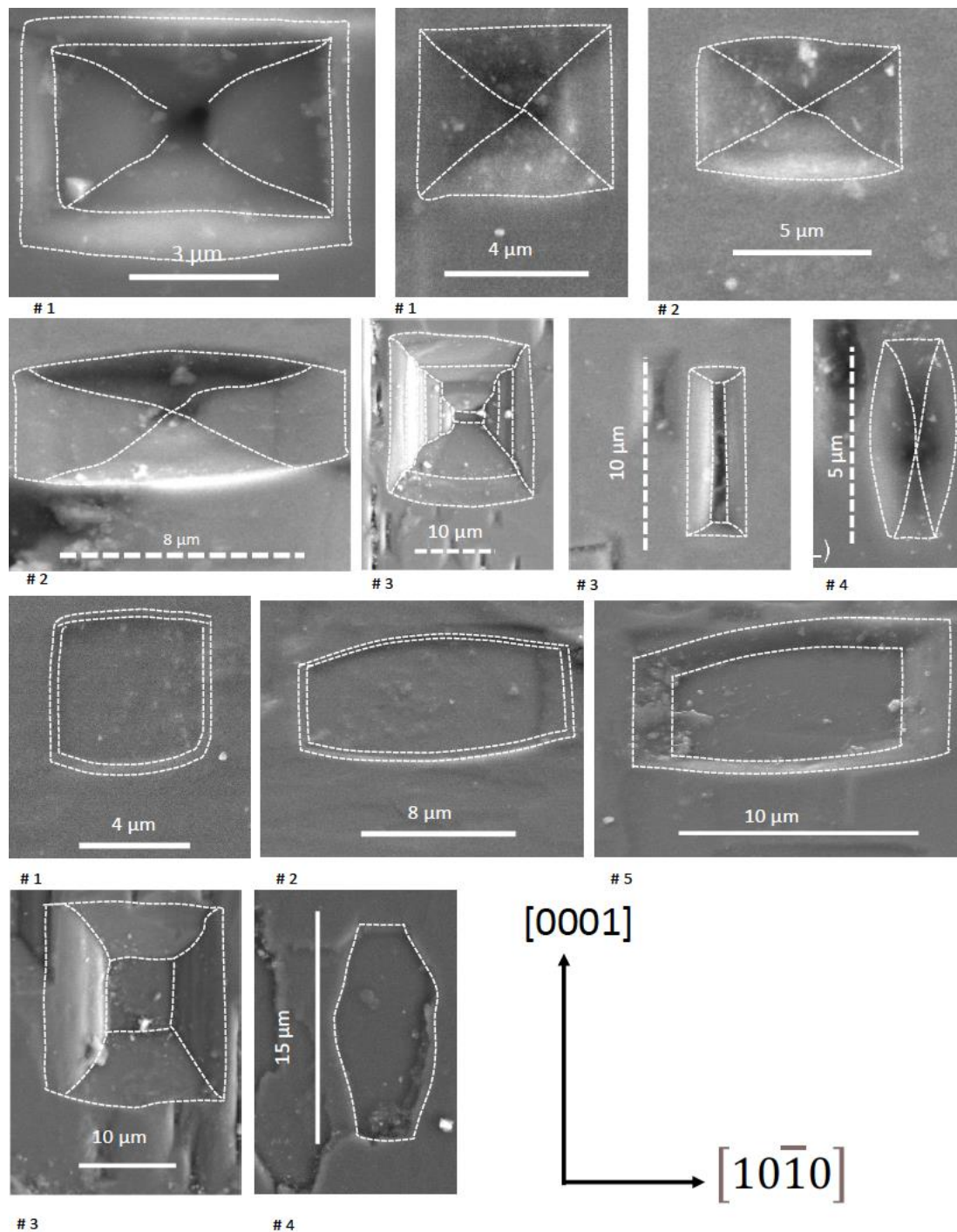


**Figure 13.** Summary of the outline (highlighted with dashed lines) of EP on the first-order prism. They are P-type (upper part) and F-type (lower part), square or mostly elongated perpendicular to the  $c$ -axis, but also parallel to it, and often with slightly curved outlines. They are commonly in the order of 5–10  $\mu\text{m}$  wide. One example of the P-type in crystal #3 (second row) shows preferred dissolution with a bottom, elongated in  $c$ -direction.

The variable shape of EP on prism faces (Fig. 13) indicates slight variations in dissolution rates in the two main directions  $[0001]$  and  $[10\bar{1}0]$ . However, as estimated from their size, overall dissolution

was minor. The rare EP with strong elongation in  $[0001]$  (Fig. 4h) are similar to EP obtained on hydrothermally grown beryl crystals after etching, where etching occurred on gas-liquid inclusions on the first-order prism (Dem'yanets and Ivanov-Schitz, 2009).

In summary, the growth structures and the dissolution structures indicate preferred growth in  $c$ -direction with the formation of indentations on  $(0001)$ , wedge-shaped features on the second-order prism instead of a flat surface due to varying growth rates in different directions, similar to the conical growth. Dissolution is minor and follows the features created by growth: EP are arranged in chains on dislocation bundles. In line with our observations, Schmetzer and Martayan (2023) described the large and deep open cavities on  $(0001)$  of the *vaso*-type emeralds from Colombia as a growth feature, whereas Pignatelli et al. (2022) argued for etch pits.

### 4.3 Chemical zoning

The sector zoning, shown in the Colombian emeralds of this study, results from preferential incorporation of elements in specific growth directions on their respective growth surfaces with different local equilibria at different faces, and these differences are preserved in the crystal bulk. Because the crystals are short prismatic with an aspect ratio near one (Table 1), the final, overall growth rates in  $a$  and  $c$  are similar (except for the long-prismatic crystal #2). However, the rate of incorporation of certain elements changes, as the sector visibility can be quite distinct for different elements. Sector zoning is well developed in magmatic and metamorphic crystals — especially well visible in crystals with a prismatic shape — such as clinopyroxene, tourmaline, andalusite (variety chiastolite) and many others (e.g. van Hinsberg et al., 2006). At high temperature and in crystals and for elements with high diffusion rates, these differences can be equilibrated. However, at low temperature diffusion is negligible in silicates, as is the case for the Colombian beryls with a formation temperature near 300–350°C. Hexagonal beryl develops a  $c$ - and an  $a$ -sector in the growth directions  $[0001]$  and  $[10\bar{1}0]$ , (Fig. 7). The trace of the sector boundaries in 2D presents information about relative growth rates in the sectors (Philpotts and Ague, 2009); straight boundaries indicate no change, curved boundaries indicate continuous changes, and serrate boundaries irregularly changing relative growth rates. The sector zoning in the Colombian emeralds is well visible in the main substitution  $^{VI}\text{Mg} + ^{\text{channel}}\text{Na} + \text{H}_2\text{O II} = ^{VI}\text{Al} + ^{\text{channel}}\square$ , and also in the substitution of chromophores for Al (Figs 8, 11). Aluminium is enriched in the  $a$ -sector, together with  $\text{H}_2\text{O I}$ , whereas Mg and Na are enriched in the  $c$ -sector together with  $\text{H}_2\text{O II}$  (Fig. 12b), consistent with the position of Na in the neighbourhood of  $\text{H}_2\text{O II}$  (Fig. 14).



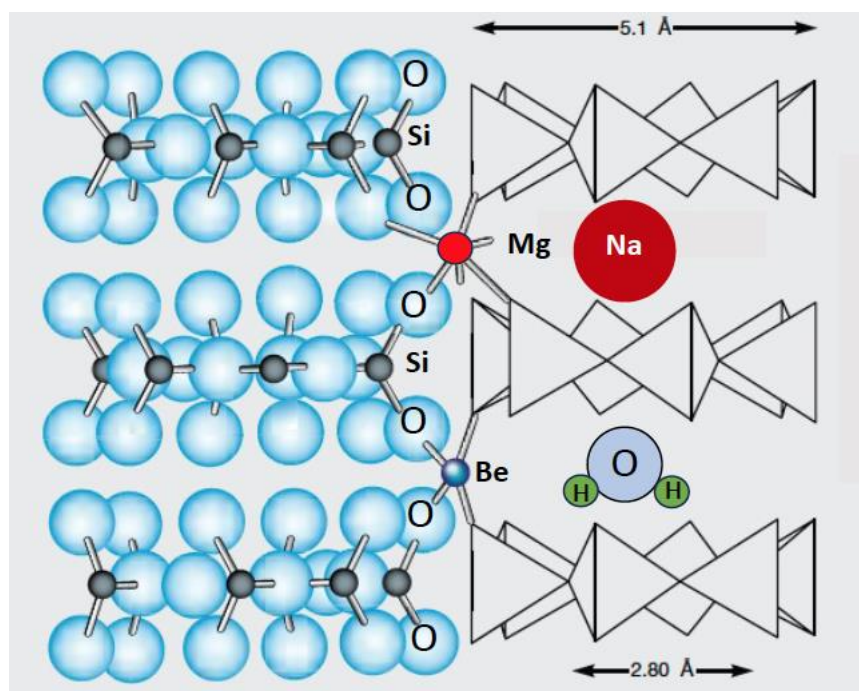


**Figure 14.** Projection of the beryl structure illustrating the 6-membered silica rings, which form channels parallel to the *c*-axis (adopted from Pignatelli et al., 2015). Local charge balance requires Na near to Mg, when it replaces <sup>VI</sup>Al, and the H<sub>2</sub>O molecule in the next vacancy orients its H-H-vector perpendicular to the *c*-axis (H<sub>2</sub>O II).

Growth bands in zoning can occur because of a gap in supply of an element and indicate an element hiatus. It is known in pegmatitic beryls as a characteristic defect (Scandale et al., 1990) and in Colombian emeralds (Pignatelli et al., 2022; Schmetzer and Martayan 2023). Such gaps were observed in the redox-sensitive elements V, Cr, and Fe in crystals #1 and 3 (Figs 8, 9). However, they are restricted to the *c*-sector, and thus, indicate only a preference of incorporation of these elements in one growth direction, not a general gap in availability of these elements. This is different to the case in the emeralds from Eidsvoll, Norway (Loughrey et al. 2013) with colour zoning in stripes parallel to *c*, and in the Emmaville occurrence, Australia (Loughrey et al. 2012) with colour zoning in bands parallel to the *a*-axis. It is also different from Cr- and V-rich overgrowths on the trapiche emeralds from Colombia (Pignatelli et al., 2015), which clearly indicate a gap in supply of elements. In the emeralds from Kruta Balka, Ukraine, Cr also shows common oscillatory growth zoning with stripes parallel to the major growth directions (Franz et al., 2020), indicating growth controlled by diffusion in the fluid/melt reservoir. This model is obviously not applicable to the Colombian emeralds investigated here.

An asymmetric growth is seen in the distribution of V, Cr and Fe in crystal #1. Such a growth feature was postulated for the growth of hydrothermal-pegmatitic beryl with a horse-shoe shape (Graziani et



al., 1981), for emeralds from Colombia (Pignatelli et al., 2022), for sector-zoned garnet from a hydrothermal-pegmatitic transition in pegmatoids from the Bohemian Massif, Austria (Kohn et al., 2024), and for lawsonite in veins of the Schistes Lustrés in the Western Alps (Lefeuvre et al., 2024). It might be a more common feature in vein minerals than known before.

Serrate sector boundaries result from changes in the growth rate, with preferred incorporation of elements into the  $a$ - and the  $c$ -sector, and again is not necessarily a result of a limited supply of these elements. Serrate boundaries are best developed in V in crystals #2 and #4 (Fig. 8), but the detailed mapping by EMPA shows that they are also very prominent in all crystals in Al, Na and Mg, due to the substitution  $^{VI}\text{Mg}^{+\text{channel}}\text{Na} = ^{VI}\text{Al}^{+\text{channel}}\square$  (Fig. 9). The sector boundaries are irregular, oblique to the  $a$ - or  $c$ -axis, but with straight borders. However, it does not follow a low-indexed crystal face, but changes the angle of the different zones (shown as stripes in Mg in crystals #1 and #2, producing in the 2D-maps triangles in concentration in crystals #2 and #5, Fig. 9). The variable direction of the sector boundaries and of the stripes rich in Mg+Na mimics the variable direction of the EP chains, corresponding to dislocation bundles, on the prism faces. Graziani et al. (1981) concluded, on the basis of X-ray tomography investigations on pegmatitic beryl, that dislocation bundles are the centres, where the crystal grew in opposite directions, meeting in a straight boundary, which is similar to the observations on the Colombian emeralds.

## 5 Summary and Conclusions

The emerald crystals, investigated in this study, show features not observed in beryls from other localities: a high density of defects, resulting in etch pits aligned in chains, and a substitution  $^{VI}\text{Mg}^{+\text{channel}}\text{Na} + \text{H}_2\text{O} \parallel = ^{VI}\text{Al}^{+\text{channel}}\square$  oriented in a pattern parallel and oblique to the  $c$ -axis. These observations are in line with the growth model presented by Pignatelli et al. (2015) for sector-zoned trapiche emeralds; in the fold-and-thrust belt of the western Cordillera in Colombia, veins opened during thrusting at low-grade metamorphic conditions. We conclude that the here investigated small crystals, grew in the abruptly filled veins from a single batch of fluid from the schist, a confined fluid reservoir. Due to the rapid pressure drop and resulting high oversaturation, the crystals grew and there are no indications for further supply of fluid. In a closed system, changes in parameters such as pH, oxygen fugacity and concentration of trace elements are much more important than in a buffered open system or in a system with a large reservoir such as a magma chamber.

The growth features observed in the emerald crystals differ from those predicted by Raleigh fractionation, which would instead show a smooth and regular shape of core-rim zoning, or with oscillatory zoning due to a diffusion process from the fluid to the crystal-fluid/melt interface. A

closed system behaviour is, however, only valid for our observations on the small investigated crystals. In contrast, some of the trapiche emeralds (Pignatelli et al., 2015) clearly show a second stage of growth with new, Cr- and V-rich fluids.

Directed flow from the matrix into the vein might have resulted in asymmetric content in trace elements, which is rapidly incorporated into the growing crystal without homogenization in the fluid. This process might be more common than described until now and can have important implications for vein minerals in general, particularly when used for age determinations or if they are used as indicators for enrichment processes of critical elements.

The confined reservoir of fluids and absence of clear indications for further supply of fluids also inhibits significant post-growth dissolution, as the fluid would remain beryl-saturated. In the Colombian emeralds, dissolution phenomena such as EP are minor, but quite distinct from what can be observed in pegmatitic beryls. The arrangement in chains is unique and it might be worth checking other vein minerals for this feature.

**Author contribution.** GF idea, data acquisition EMPA, SEM, writing of first draft; VK IR, writing; FS  $\mu$ XRF, writing; JN EMPA; UG SEM

#### **Acknowledgements.**

Alexander-von-Humboldt-Stiftung and Akademisches Auslandsamt Technische Universität Berlin supported Vladimir Khomenko during his stays in Berlin, and financial support by DFG fund FR557/34-1 is gratefully acknowledged. Thorough reviews by Vincent van Hinsberg, two anonymous reviewers and editorial comments and handling by Barb Dutrow were of great help to improve the manuscript.

**Supplementary material.** The supplementary material for this article can be found at GFZ data services <https://doi.org/10.5880/fidgeo.2025.006>

**Competing interests.** The authors declare none.

## References

- Aurischio C., Fioravanti G., Grubessi O. and Zanazzi P.F. (1988) Reappraisal of the crystal chemistry of beryl. *American Mineralogist*, 75, 826-837.
- Bartoshinskiy Z.V., Matkovskiy O.I. and Srebrodolskiy B.I. (1969) Accessory beryl from chamber pegmatites of Ukraine. *Mineralogical Sbornik*, 23, N4, 382-397 (in Russian).
- Beig M.S. and Lüttge, A. (2006) Albite dissolution kinetics as a function of distance from equilibrium: Implications for natural feldspar weathering. *Geochimica and cosmochimica acta*, 70, 1402-1420. doi:10.1016/j.gca.2005.10.035.
- Demianets L.N., Ivanov-Shitz A.K. and Gainutdinov R.V. (2006) Hydrothermal growth of beryl single crystals and morphology of their singular faces. *Inorganic materials*, 42(9), 989-995. doi.org/10.1134/S0020168506090111.
- Dem'yanets L.N. and Ivanov-Schitz A.K. (2009) Beryl: Regeneration crystal growth and morphology of regeneration surfaces. *Journal of Surface Investigation, X-ray, Synchrotron and Neutron Techniques*, 3(6), 881-887, doi.org/10.1134/S1027451009060068.
- Franz G., Vyshnevskiy O., Taran M., Khomenko V., Wiedenbeck M., Schiperski F. and Nissen J. (2020) A new emerald occurrence from Kruta Balka, Western Peri-Azovian region, Ukraine: Implications for understanding the crystal chemistry of emerald. *American Mineralogist* 105(2), 162-181. doi.org/0021-8898/81/040241-06501.00
- Franz G., Vyshnyevskiy O., Khomenko V., Lyckberg P., Wiedenbeck M. and Gernert U. (2023) Etch pits in heliodor from the Volyn pegmatites, NW Ukraine - a diagnostic feature. *Gems & Gemology*, 59, 324-339, doi.org/10.5741/GEMS.59.3.324.
- Franz G., Schiperski F., Khomenko V., Gernert, U. and Nissen J. (2025) Columbian emeralds – internal and external growth and dissolution features (ex 2023.021). GFZ Data Services. <https://doi.org/10.5880/fidgeo.2025.006>
- Graziani G., Scandale E. and Zarka A. (1981) Growth of a beryl single crystal – history of the development and the genetic medium. *Journal of Applied Crystallography*, 14, 241, 246.
- Henry D.J. and Dutrow B.L. (1996) Metamorphic tourmaline and its petrologic applications. In: Grew E.S., Anovitz L.M. (Eds.), *Boron: Mineralogy, Petrology, and Geochemistry. Reviews in Mineralogy*, 33, 505-557.
- Henry, R.E., Groat, L.A., and Evans, R.J. (2022) Crystal-chemical observations and the relation between sodium and H<sub>2</sub>O in different beryl varieties. *Canadian Mineralogist*, 60, 626-675, doi: 10.3749/canmin.2100050
- Herzberg C. (1945) *Infrared and Raman spectra of polyatomic molecules*. Vol. 2, van Nostrand, Inc. New York.
- Khomenko V. and Langer K. (2005) Carbon oxides in cordierite channels: Determination of CO<sub>2</sub> isotopic species and CO by single crystal IR spectroscopy. *American Mineralogist*, 90, 1913-1917. doi: 10.2138/am.2005.1963
- Kohn M. (2014) *Geochemical zoning in metamorphic minerals. Treatise in Geochemistry*, Elsevier, 3, 229-261.

- Kohn V., Alifirova T., Daneu, N. Griffiths T.A., Libowitzky E., Linner M., Ertl A., Abart R. and Habler G. (2024) Directed growth of a sector-zoned garnet in a pegmatoid from the Bohemian Massif, Austria. *Lithos*, 466-467, 107461, doi.org/10.1016/j.lithos.2023.107461
- Lefeuve B., Dubacq B., Verlaquet A., Herviou C., Walker S., Caron B., Baxter E. and Agard P. (2024) Disentangling the compositional variations of lawsonite in blueschist-facies metasediments (Schistes Lustrés, W. Alps). *Contributions to Mineralogy and Petrology*, 179(3), 25, doi.org/10.1007/s00410-024-02104-5.
- Libowitzky, E., and Rossman, G. R. (1997). An IR absorption calibration for water in minerals. *American Mineralogist*, 82(11-12), 1111-1115.
- Loughrey L., Groat D., Jones P., Millsteed P. and Main A. (2012) Emmaville-Torrington emerald deposit. *Central European Journal of Earth Sciences*, 4, 287-299 doi:10.2478/s13533-011-0056-9.
- Loughrey L., Marshall D., Ihlen P. and Jones P. (2013) Boiling as a mechanism for colour zonations observed at the Byrud emerald deposit, Eidsvoll, Norway: fluid inclusion, stable isotope and Ar–Ar studies. *Geofluids*, 13(4), 542-558.
- Lu D., Jiang Q., Ma X., Zhang Q., Fu X. and L. Fan (2022) Defect-related etch pits on crystals and their utilization. *Crystals* 12(11).
- Lüttge A. (2005) Etch pit coalescence, surface area, and overall mineral dissolution rates. *American Mineralogist*, 90, 1776-17873. doi: 10.2138/am.2005.1734.
- Philpotts A. and Ague J. (2009) *Principles of igneous and metamorphic petrology*. 2<sup>nd</sup> ed, Cambridge University Press, Cambridge (UK), ISBN 978-0-52188006-0.
- Pignatelli I., Guilianni G., Ohnenstetter D., Agrosi G., Mathieu S., Morlot C. and Branquet Y. (2015) Colombian trapiche emeralds: Recent advances in understanding their formation. *Gems & Gemology*, 51, 222-259, doi.org/10.5741/GEMS.51.3.222.
- Pignatelli I., Morlot C., Salsi L., Giuliani G. and Martayan G. (2022) Colombian emerald oddities: Review and formation mechanisms. *The Journal of Gemmology*, 38(1), 26-43, doi.org/10.3190/jgeosci.314.
- Renfro, N., Smith, T., Koivula, J.I., McClure, S.F., Schumacher, K., and Shigley, J.E. (2023) Micro-features of beryl. *Gems & Gemology*, 59, 484-485, doi.org/105741/GEMS.59.4.484
- Rubin A.E., Cooper K.M., Till C.B., Kent A.J.R., Costa F., Bose M., Gravley D., Deering C. and Cole J. (2017). Rapid cooling and cold storage in a silicic magma reservoir recorded in individual crystals. *Science*, 356, 1154-1156, doi.org/10.1126/science.aam8720.
- Saeseaw, S., Refro N.D., Palke A.C., Sun, Z., and McClure S.F. (2019) Geographic origin determination of emerald. *Gems & Gemology*, 55, 614-646, doi.org/10.5741/GEMS.55.4.614
- Scandale E., Lucchesi S., and Graziani G. (1990) Growth defects and growth marks in pegmatitic beryls. *European Journal of Mineralogy*, 2, 305-311.
- Schwarz, D., and Schmetzer, K. (2002). The definition of emerald: The green variety of beryl colored by chromium and/or vanadium. *Emeralds of the World*, 74-78.

- Schmetzer K. and Martyan G. (2023) Morphology of Colombian emerald: Some less common cases and their growth and dissolution history. *Gems & Gemology*, 59, 46-71, doi.org/10.5741/GEMS.59.1.46.
- Sunagawa I. (2005) *Crystals – growth, morphology, and perfection*. Cambridge University Press, Cambridge UK, ISBN-13 978-0-511-11345-1, pp 308.
- Sunagawa I. and Urano A. (1999) Beryl crystals from pegmatites: morphology and mechanism of crystal growth. *Journal of Gemmology*, 26, 521-53.
- Van Hinsberg V.J., Schumacher J.C., Kearns S., Mason P.R.D., and Franz G. (2006) Hour glass zoning in metamorphic tourmaline and resultant major and trace element fractionation. *American Mineralogist*, 91, 717-728.
- Wood D.L., and Nassau K. (1967) Infrared spectra of foreign molecules in beryl. *J. Chem. Phys.*, 47, 2220-8.